Human Molecular Genetics, 2012, Vol. 21, No. 26 **5484–5499**
doi:10.1093/hmg/dds393
Advance Access published on September 21, 2012

An inherited *TUBB2B* mutation alters a kinesin-binding site and causes polymicrogyria, CFEOM and axon dysinnervation

Gustav Y. Cederquist[1,†], Anna Luchniak[7,†], Max A. Tischfield[1,‡,¶], Maya Peeva[1,‡], Yuyu Song[1,‡], Manoj P. Menezes[9,12], Wai-Man Chan[1,13], Caroline Andrews[1,13,14], Sheena Chew[1,13,14], Robyn V. Jamieson[10,12], Lavier Gomes[12,15], Maree Flaherty[11], Patricia Ellen Grant[2,3,14], Mohan L. Gupta Jr[8,*] and Elizabeth C. Engle[1,4,5,6,13,14,*]

[1]Department of Neurology, [2]Department of Medicine, and [3]Department Radiology, Boston Children's Hospital, Boston, MA, USA, [4]Department of Ophthalmology, [5]FM Kirby Neurobiology Center, and [6]Mantor Center for Orphan Disease Research, Boston Children's Hospital, Boston, MA, USA, [7]Department of Biochemistry and Molecular Biology, and [8]Department of Molecular Genetics and Cell Biology, University of Chicago, Chicago, IL, USA, [9]The Institute for Neuroscience and Muscle Research, [10]Department of Genetics, and [11]Department of Ophthalmology, The Children's Hospital at Westmead, Westmead, Sydney, NSW, Australia, [12]Sydney Medical School, University of Sydney, Camperdown, Sydney, NSW, Australia, [13]Howard Hughes Medical Institute, Chevy Chase, MD, USA, [14]Harvard Medical School, Boston, MA, USA and [15]Department of Radiology, Westmead Hospital, Westmead, Sydney, NSW, Australia

Received June 6, 2012; Revised September 7, 2012; Accepted September 14, 2012

Microtubules are essential components of axon guidance machinery. Among β-tubulin mutations, only those in *TUBB3* have been shown to cause primary errors in axon guidance. All identified mutations in *TUBB2B* result in polymicrogyria, but it remains unclear whether *TUBB2B* mutations can cause axon dysinnervation as a primary phenotype. We have identified a novel inherited heterozygous missense mutation in *TUBB2B* that results in an E421K amino acid substitution in a family who segregates congenital fibrosis of the extraocular muscles (CFEOM) with polymicrogyria. Diffusion tensor imaging of brains of affected family members reveals aberrations in the trajectories of commissural projection neurons, implying a paucity of homotopic connections. These observations led us to ask whether axon dysinnervation is a primary phenotype, and why the E421K, but not other, TUBB2B substitutions cause CFEOM. Expression of exogenous Tubb2b-E421K in developing callosal projection neurons is sufficient to perturb homotopic connectivity, without affecting neuronal production or migration. Using *in vitro* biochemical assays and yeast genetics, we find that TUBB2B-E421K αβ-heterodimers are incorporated into the microtubule network where they alter microtubule dynamics and can reduce kinesin localization. These data provide evidence that *TUBB2B* mutations can cause primary axon dysinnervation. Interestingly, by incorporating into microtubules and altering their dynamic properties, the E421K substitution behaves differently than previously identified TUBB2B substitutions, providing mechanistic insight into the divergence between resulting phenotypes. Together with previous studies, these findings highlight that β-tubulin isotypes function in both conserved and divergent ways to support proper human nervous system development.

*To whom correspondence should be addressed at: CLS14074, Boston Children's Hospital, 300 Longwood Ave, Boston, MA 02115, USA. Tel: +1 6179194030; Fax: +1 6179192769; Email: elizabeth.engle@childrens.harvard.edu (E.C.E.); CLSC 218B, University of Chicago, 920 E 58th St, Chicago, IL 60637 USA. Tel: +1 7738341376; Fax: +1 7737023172; Email: mlgupta@uchicago.edu (M.L.G.).
†Equally contributing co-first authors.
‡Equally contributing co-second authors.
¶Present address: Department of Molecular Biology and Genetics, Johns Hopkins Medical School, Baltimore, MD, USA.

© *The Author 2012. Published by Oxford University Press. All rights reserved.*
For Permissions, please email: journals.permissions@oup.com

Downloaded from http://hmg.oxfordjournals.org/ at Serials Department on January 4, 2013

INTRODUCTION

The structural and functional integrity of the microtubule cytoskeleton is critical to human nervous system development. Microtubules are dynamic polymers that assemble from αβ-tubulin heterodimers and support diverse functions inside the cell. Humans harbor nine genes that encode distinct β-tubulin monomers, termed isotypes. Because isotype sequences are conserved across evolution (1–3) and isotypes differ in their spatial and temporal expression (2,4–7), it has been suggested that distinct isotype compositions may confer unique properties to the microtubule polymer (8,9). However, the role of isotype diversity in supporting the multitude of microtubule-related functions remains unclear.

Human genetics has begun to provide insight into the role of specific tubulin isotypes. Twenty-three unique human heterozygous missense mutations in genes that encode β-tubulin isotypes TUBB2B and TUBB3 have been reported (10–14). Phenotype–genotype analyses support correlations between the mutated isotype and the resulting neurological phenotypes (11,15). Mutations altering *TUBB3*, which is expressed in post-mitotic neurons but not glia, segregate into two distinct phenotypic groups (11,13,15). Eight reported amino acid substitutions in *TUBB3* cause *c*ongenital *f*ibrosis of the *e*xtra*o*cular *m*uscles (CFEOM), a congenital disorder in which maldevelopment of cranial nerve axons leads to ptosis (drooping eye lids) and restricted eye movements (11,16–18). A subset of mutations segregate with facial weakness, intellectual and social disabilities and/or progressive sensorimotor peripheral neuropathy. Human neuroimaging revealed cranial nerve hypoplasia and a mouse model of the TUBB3 R262C substitution suggests this is due to cranial axon misguidance (11,16). This CFEOM mouse model also recapitulates the human anterior commissure and corpus callosum (CC) hypoplasia (11). Neither human neuroimaging nor mouse pathology has identified cortical lamination defects, indicating that CFEOM-causing mutations in *TUBB3* lead to primary axonal dysinnervation (11,15).

The second group of *TUBB3* mutations includes six unique amino acid substitutions that cause a spectrum of cortical dysplasias collectively termed malformations of cortical development (MCD), including gyral disorganization and simplification or polymicrogyria (PMG), a cortical dysplasia resulting from impaired neuronal migration and characterized by shallow sulci and excessive numbers of gyri on the brain surface (19). Patients with MCD have intellectual and motor disabilities and can have comitant strabismus, but do not have CFEOM. Neuroimaging revealed CC hypoplasia and misguided fiber bundles in the internal capsule, suggesting additional axon pathfinding defects (13).

Eight amino acid substitutions in TUBB2B, which is highly expressed in both neurons and glia, have been reported to cause tubulin folding defects and PMG. Affected family members also present with variable degrees of CC dysplasia (10,12). The association of PMG with mutations that result in reduced TUBB2B levels suggests that TUBB2B may be essential for proper neuronal migration (10). A newly reported *de novo TUBB2B* mutation in a single patient associates with the developmental delay in the setting of PMG and open-lip schizencephaly, and unilateral ptosis and exotropia in the setting of a thin ipsilateral oculomotor nerve (14). These findings raise the possibility that TUBB2B, like TUBB3, has a critical role in axon guidance, but it remains unclear whether accompanying axon tract abnormalities are primary defects, or if they arise secondary to severe structural brain abnormalities.

We have now identified a novel heterozygous *TUBB2B* mutation that segregates with CFEOM, bilateral PMG and a paucity of homotopic callosal connections (20). Using this mutation, we ask whether mutant *TUBB2B* alleles can cause primary axonal dysinnervation, and why only a subset of *TUBB2B* mutations cause CFEOM. By introducing this mutation into developing mouse cortical neurons in a mosaic fashion, we do not induce migratory phenotypes and PMG, but do find disruptions in homotopic connectivity, thus providing evidence of a primary axonal phenotype. Using *in vitro* and *in vivo* cellular assays, we find that αβ-heterodimers containing the E421K substitution incorporate into microtubule polymers and alter dynamic instability and specific kinesin–microtubule interactions. These molecular phenotypes differ from those caused by *TUBB2B* mutations that do not result in CFEOM, providing an explanation for the divergence in their respective phenotypes.

RESULTS

A genetically undefined syndrome is characterized by CFEOM with intellectual disability

We previously reported and have now re-examined an Australian-based Caucasian family in which the mother (I:2) and two (II:2 and II:3) of four children have CFEOM and intellectual disability (20). The mother (44 years) and two affected daughters (21 and 20 years) display CFEOM with no significant changes since the initial report. All have bilateral ptosis (drooping eyelids), both eyes fixed in downgaze, and a compensatory chin-up head position. Vertical eye movements are severely limited with jerky convergent movements on attempted elevation, and horizontal movements are variably restricted. Both daughters showed significant intellectual disability (<1st percentile) in recent neuropsychological testing and had head circumferences <2nd percentile, whereas their heights and weights fell in the 10–50th percentiles. The mother, though not formally assessed, was previously reported to have low to average intellectual function (20). One daughter has difficulty modulating her behavior. The remaining exams including slit lamp, fundoscopy, pupillary reaction, non-oculomotor cranial nerve function, motor strength and tone, deep tendon reflexes, sensory modalities and coordination were normal. None have lost developmental milestones, experienced seizures or developed symptoms of peripheral neuropathy. Nerve conduction studies of the older daughter were normal (Fig. 1A).

Previous magnetic resonance imaging (MRI) scans of the daughters at ages 4 and 9 showed variable hypoplasia of affected extraocular muscles, and imaging of the mother at the age of 26 had revealed thinned medial and lateral rectus muscles, and hypoplastic superior rectus and levator palpebrae superioris muscles, consistent with CFEOM (20). The daughters' earlier scans, as well as repeat brain MRI scans at the age

Downloaded from http://hmg.oxfordjournals.org/ at Serials Department on January 4, 2013

A

Clinical Phenotypes	Head circumference	Microcephalic
	Intellectual disability	Yes
	Epilepsy	No
	Motor function	Normal
	Eye movements	CFEOM
	Facial strength	Normal
	Peripheral neuropathy	No
Neuroimaging	Cortical gyral pattern	Bilateral PMG
	Location of PMG	Perisylvian to diffuse
	Basal ganglia	Asymmetric dysmorphic
	Corpus callosum	Body hypoplasia
	Cerebellum	Mild dysplasia
	Brainstem	Grossly normal
	Ocular muscles	Hypoplastic MR, LR, SR, SO

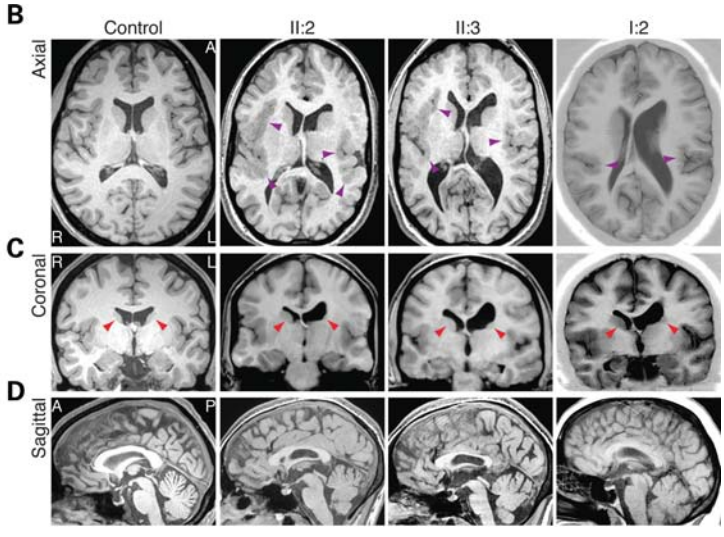

Figure 1. A genetically undefined syndrome characterized by CFEOM and intellectual disability. (**A**) Chart summarizing clinical and neuroradiological findings of affected family members. (**B**) Axial views show the extent of PMG in patients. PMG is diffuse and bilateral in II:2 and II:3 and primarily perisylvian in I:2 (purple arrowheads). (B and **C**) Axial and coronal views show basal ganglia dysmorphisms. There is marked dysplasia of the left caudate head, and a poorly defined putamen when compared with the right (red arrowheads). In addition, there are asymmetric white matter tract abnormalities, with poor fasciculation of the left internal capsule and left ventricular dilation. (**D**) Sagittal views show thinning of the CC body, whereas the genu is comparably less hypoplastic. I:2 (affected mother), II:2 (affected older daughter) and II:3 (affected younger daughter) refer to pedigree positions in Figure 2. CFEOM, congenital fibrosis of the extraocular muscles; PMG, polymicrogyria; MR, medial rectus; LR, lateral rectus; SR, superior rectus; SO, superior oblique; L, left hemisphere; R, right hemisphere; A, anterior; P, posterior.

of 19 (II:3) and 20 (II:2), revealed prominent diffuse bilateral PMG (Fig. 1B), dilation of the left lateral ventricle (Fig. 1B and C) with hypoplasia of the body of the ipsilateral caudate nucleus (Fig. 1C), and fusion of an enlarged caudate nucleus head with the underlying putamen (20). Both have a thin CC body with comparatively normal looking genu (Fig. 1D). Retrospective review of the mother's scan (I:2) also revealed mild bilateral perisylvian PMG in addition to the previously reported ventricular and caudate asymmetries (Fig. 1B and C).

CFEOM and intellectual disability segregate with a heterozygous mutation in *TUBB2B*

Haplotype analysis previously revealed co-segregation of the family's autosomal dominant phenotype with polymorphic markers flanking the *FEOM1* and *FEOM3* loci (20). Thus, we sequenced the disease genes at these loci, *KIF21A* and *TUBB3*, but did not identify disease-associated variants. Next, taking a candidate approach, we sequenced *TUBA1A* and *TUBB2B* and identified a heterozygous c.1261G>A nucleotide substitution in exon 4 of *TUBB2B* that co-segregated with the affliction status and with a haplotype flanking the *TUBB2B* locus (Fig. 2A and B). The *TUBB2B* variant was absent from 336 control individuals, dbSNP (http://www.ncbi.nih.gov/SNP), the 1000 Genomes Project (http://browser.1000genomes.org/index.html) and the NHLBI ESP Exome Variant Server (http://evs.gs.washington.edu/EVS/). No disease variants were found in *TUBA1A*.

The *TUBB2B* c.1261G>A mutation is predicted to substitute a positively charged lysine for a negatively charged glutamic acid at residue 421 of TUBB2B (E421K). E421 is evolutionarily conserved across β-tubulin isotypes from yeast to human (Fig. 2C). Along with E410 and D417, it is located in the C-terminal H12 α-helix of β-tubulin and is crucial for kinesin–microtubule interactions (21–24) (Supplementary Material, Fig. S1). This is remarkable, as we previously identified CFEOM3 disease-causing amino acid substitutions at TUBB3 residues E410 and D417 (11).

To estimate the frequency of *TUBB2B* variants underlying CFEOM, we sequenced *TUBB2B* in 25 additional families and 80 sporadic individuals with mutation-negative CFEOM or other vertical congenital cranial dysinnervation disorder (CCDD) phenotypes, none of who were known to have PMG, and did not identify any additional disease-associated variants. Together, these data build and expand on a previous case-report that identified a *de novo TUBB2B* CFEOM mutation in a single individual (14), but also suggest that *TUBB2B* mutations are a rare cause of CFEOM.

Abnormal intracortical homotopic connectivity is associated with TUBB2B-E421K

Using diffusion tensor imaging (DTI) data from both daughters, we performed diffusion tractography to interrogate the long-range coherence of the CC, the brain's major interhemispheric/commissural white matter pathway. Consistent with the structural T1 MRI scans, DTI scans showed a mild to moderate paucity of fibers in the CC body, whereas the genu was less affected. Moreover, the directionality of commissural fibers in the CC body was strikingly abnormal. While CC fibers normally display left–right directionality, visualized as red tracks, many commissural fibers in the affected individuals were labeled green, indicating a dominant anterior to posterior directionality from which we can infer a paucity of homotopic connections (Fig. 3A and B). While the

Downloaded from http://hmg.oxfordjournals.org/ at Serials Department on January 4, 2013

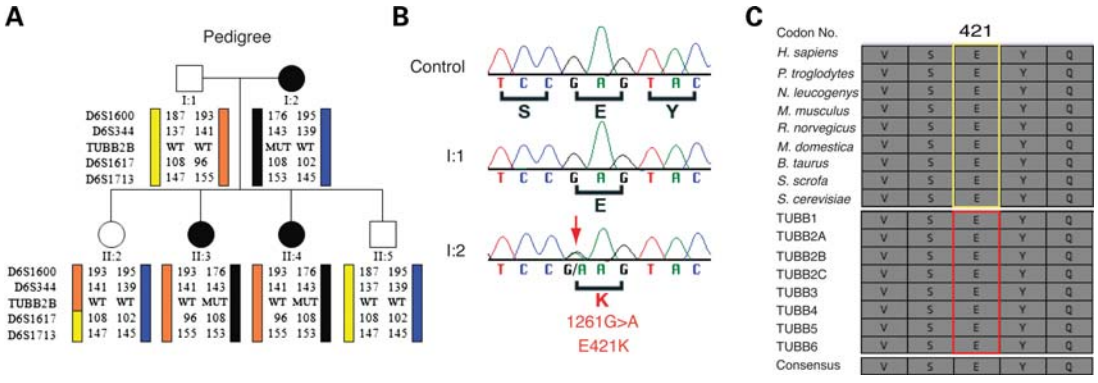

Figure 2. Heterozygous *TUBB2B* 1261G>A mutation (E421K) segregates with CFEOM and PMG. (**A**) Schematic of pedigree and targeted linkage analysis on chromosome 6 identifies a haplotype flanking the *TUBB2B* locus that segregates with the disease with complete penetrance. Pedigree members are denoted by circles (females) and squares (males) and by generation and position. Solid shapes indicate clinically affected individuals. 'MUT' indicates presence of the *TUBB2B* mutation, whereas 'WT' indicates the wild-type *TUBB2B* allele. (**B**) Targeted sequencing of *TUBB2B* coding exons and splice sites reveals a 1261G>A (E421K) heterozygous missense mutation (red arrow) that is found in all affected and not in unaffected individuals from the pedigree. (**C**) The E421 residue is strictly conserved across eukaryotic Tubb2b homologues (top, yellow box) and human β-tubulin isotypes (bottom, red box).

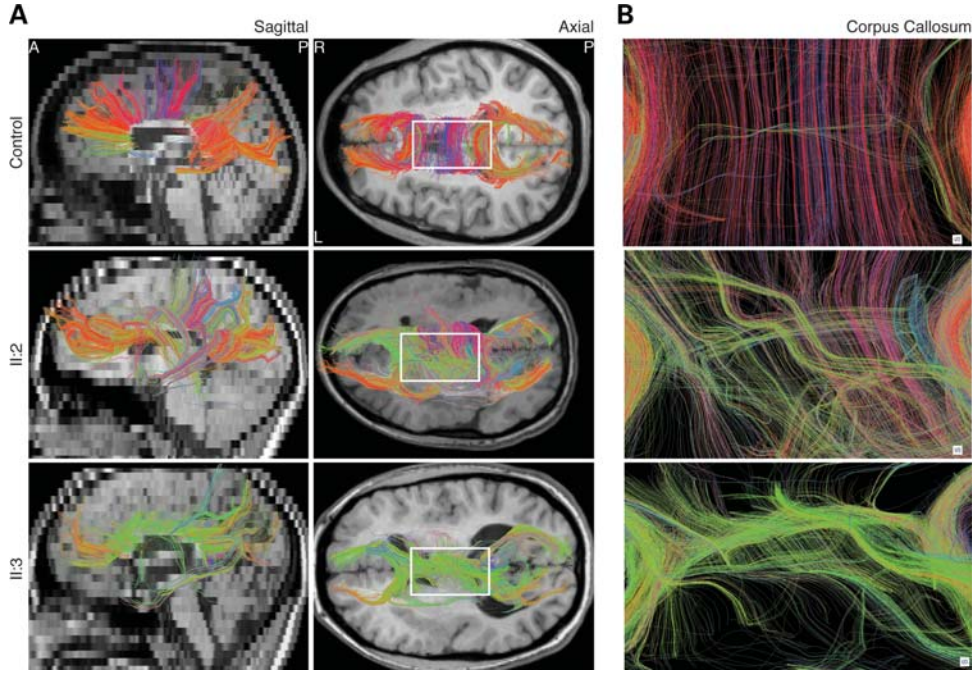

Figure 3. Abnormal homotopic connectivity associated with TUBB2B-E421K. Human DTI images segmenting commissural fibers of the CC. (**A**) Sagittal and axial views show that TUBB2B-E421K patients have a paucity of commissural fibers in the CC body, consistent with structural MRI findings. Furthermore, while many fibers in the healthy control are reconstructed with red color, many commissural fibers in TUBB2B-E421K patients are colored green, indicating a lack of normal homotopic connectivity. (**B**) Zoom in of the boxed region in (A) confirms that homotopic connectivity is disrupted in patients. CC, corpus callosum. Color coding: red, left–right; green, anterior–posterior; blue, superior–inferior.

overwhelming majority of control CC fibers intersected the cortical midline perpendicularly, fibers in affected individuals traversed through the midline at oblique angles (Fig. 3B). Furthermore, fiber bundles in the control were spaced in regular intervals, whereas fibers in the affected daughters clustered irregularly, sometimes forming thick bundles (Fig. 3B). This pattern of commissural fiber dysinnervation was not seen in nine genetically undefined PMG patients without CFEOM (Supplementary Material, Fig. S2), suggesting that disrupted homotopic intracortical connections associated with TUBB2B-E421K were not secondary to cortical dysplasia, and may be a primary defect.

TUBB2B-E421K perturbs homotopic connectivity across the midline

To investigate how the TUBB2B-E421K substitution leads to abnormal homotopic connectivity, we introduced the mutant allele into a small number of wild-type callosal projection neurons (CPN) via *in utero* electroporation of E15.5

Downloaded from http://hmg.oxfordjournals.org/ at Serials Department on January 4, 2013

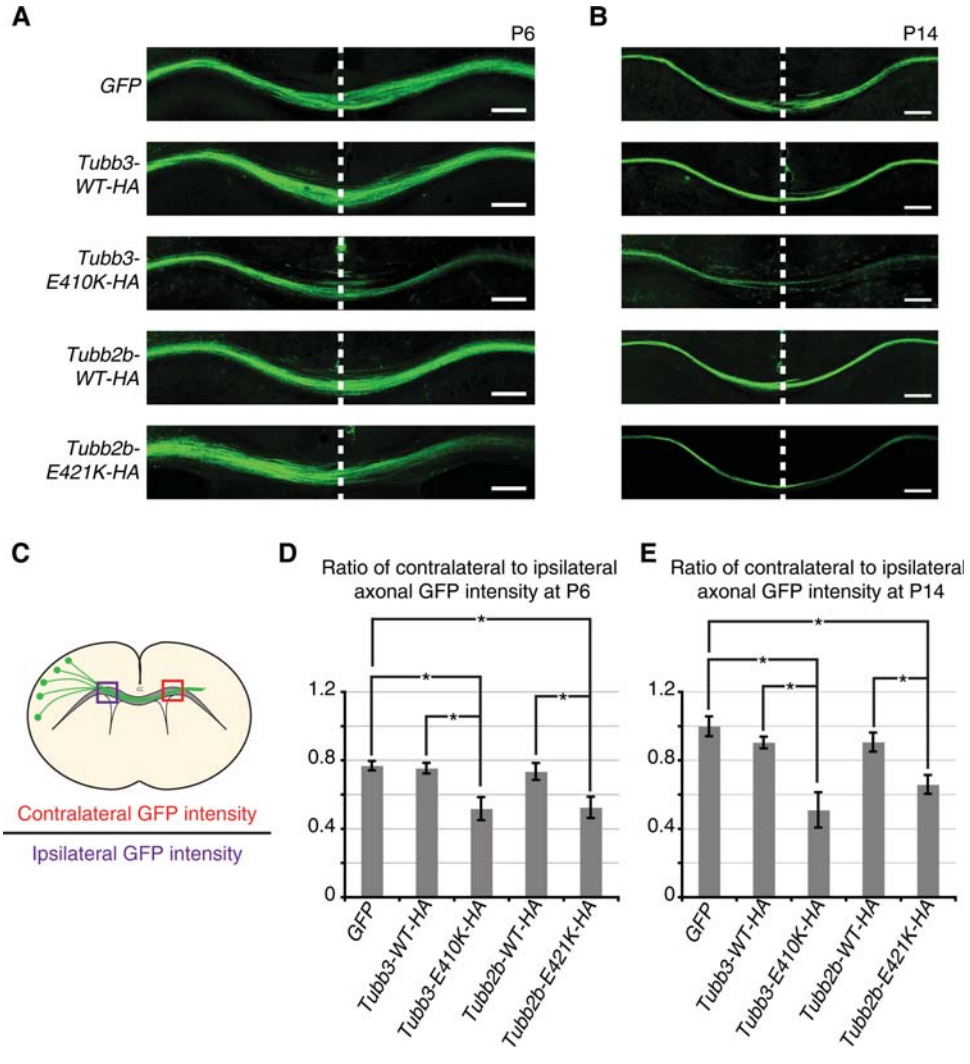

Figure 4. Tubb2b-E421K-HA perturbs homotopic connectivity at the cortical midline. Fluorescent micrographs and quantification of axonal GFP intensity in the corpus callosum of electroporated mouse brains. (**A** and **B**) At P6 and P14, axonal GFP intensity is reduced in the contralateral hemisphere of brains electroporated with *Tubb3-E410K-HA* and *Tubb2b-E421K-HA* compared with GFP and WT controls. (**C**) Schematic describes quantification method. (**D** and **E**) Quantification confirms observations of reduced contralateral GFP intensity. (D) At P6, GFP = 0.77 ± 0.05, Tubb3-WT-HA = 0.73 ± 0.04, Tubb3-E410K-HA = 0.52 ± 0.14 ($P < 0.05$ compared to GFP and Tubb3-WT-HA), Tubb2b-WT-HA = 0.75 ± 0.10, Tubb2b-E421K-HA = 0.52 ± 0.11 ($P < 0.05$ compared GFP and Tubb2b-WT-HA). (E) At P14, GFP = 1.00 ± 0.08, Tubb3-WT-HA = 0.90 ± 0.06, Tubb3-E410K-HA = 0.51 ± 0.18 ($P < 0.01$ compared with GFP, and $P < 0.05$ compared with Tubb3-WT-HA), Tubb2b-WT-HA = 0.90 ± 0.10, Tubb2b-E421K-HA = 0.66 ± 0.08 ($P < 0.05$ compared with GFP and Tubb2b-WT-HA). For P6 and P14, $n = 4,3$ (GFP), $n = 3,4$ (Tubb3-WT-HA), $n = 5,4$ (Tubb3-E410K-HA), $n = 5,3$ (Tubb2b-WT-HA), $n = 4,4$ (Tubb2b-E421K-HA). Each N represents one embryo. One-way ANOVA with a *post hoc* Tukey *t*-test was used for multiple comparisons. CC, corpus callosum. Error bars represent SEM. $^*P < 0.05$. Scale bars: 200 μm.

mouse cortical progenitors. We co-electroporated constructs to express GFP-alone or GFP with either HA-tagged Tubb2b (Tubb2b-WT-HA) or Tubb2b-E421K (Tubb2b-E421K-HA). As a positive control, we used constructs expressing GFP and either Tubb3-WT-HA or Tubb3-E410K-HA, which causes primary axonal dysinnervation in humans (11) (Supplementary Material, Fig. S3A and B). We verified that all constructs produce functional tubulin that incorporates into neuronal microtubules (Supplementary Material, Fig. S3C).

To evaluate homotopic connectivity, we examined coronal sections of electroporated brains at P6 (Fig. 4A) and P14 (Fig. 4B) and compared the ratio of axonal GFP signal intensity in the contralateral CC to that in the ipsilateral CC (Fig. 4C). Since homotopic CPN acquire symmetrical connectivity across the cortical midline, axonal GFP intensity should be roughly equivalent on each side of the CC. As expected, we observed this in brains electroporated with GFP alone, and found no significant change in brains electroporated with Tubb3-WT-HA or Tubb2b-WT-HA. However, there was a significant decrease in the ratio of contralateral to ipsilateral GFP signal in brains expressing Tubb3-E410K-HA or Tubb2b-E421K-HA, compared with their respective controls at both P6 (Fig. 4D) and P14 (Fig. 4E). Since the phenotype did not resolve by P14, it is unlikely that axon outgrowth was simply delayed.

Downloaded from http://hmg.oxfordjournals.org/ at Serials Department on January 4, 2013

The observed errors in axonal pathfinding occur in the context of a largely normal cortex (Supplementary Material, Fig. S4). Overexpression of Tubb2b-E421K-HA did not affect cell-cycle exit of mitotic neuronal progenitors (Supplementary Material, Fig. S5), and did not produce migratory abnormalities (Supplementary Material, Fig. S6). In addition, neurons expressing Tubb2b-E421K-HA acquired a midline phenotype highly similar to those expressing Tubb3-E410K-HA (Fig. 4). Together, our data demonstrate that Tubb2b-E421K can cause axonal dysinnervation that is not secondary to cortical dysplasia, neuronal production or abnormal neuronal migration. Instead, the observed axonal dysinnervation, which is consistent with findings from human neuroimaging, appears to be a primary and dominant phenotype.

Tubb2b-E421K overexpression inhibits target innervation by commissural projection neurons

The consistency between human DTI and mouse electroporation results led us to explore other potential axonal deficits caused by the dominant effects of Tubb2b-E421K protein. As expected, CPN axons electroporated with GFP alone at E15.5 had traversed through the entirety of the CC and begun to innervate their most distant contralateral targets in the striatum and lateral neocortex at P6 (25) (Fig. 5). Similar patterns resulted from electroporation with *Tubb3-WT-HA* or *Tubb2b-WT-HA*. In contrast, introduction of *Tubb3-E410K-HA* or *Tubb2b-E421K-HA* resulted in decreased contralateral innervation of long-distance targets. Though many mutant axons traversed through the CC, they failed to innervate the contralateral striatum and lateral neocortex (Fig. 5B and C). These deficits did not resolve by P14 (Supplementary Material, Fig. S7), indicating that the mutant tubulin alleles prevent target innervation by homotopic projecting neurons. The reduced innervation may be a primary phenotype or may be secondary to abnormal midline crossing and pathfinding of CPN (Fig. 4).

Tubb2b-E421K perturbs the layer-specificity of ipsilateral cortical microcircuitry

In addition to long-range contralateral connectivity, CPN axons also participate in the construction of local microcircuitry. In agreement with previous studies (26), we observed that at P6, following GFP electroporation at E15.5, the large majority of ipsilateral branching of layer II/III CPN occurred in layer V, whereas little occurred in layer VI. Electroporation of *Tubb3-WT-HA* produced branching patterns comparable with the GFP-alone condition, whereas electroporation of *Tubb2b-WT-HA* produced slight, but excessive branching in layer VI. Introduction of *Tubb3-E410K-HA* or *Tubb2b-E421K-HA* resulted in more prominent and excessive branching in layer VI, at levels that were visually greater than those of the *Tubb2b-WT-HA* condition (Fig. 6A). Quantitative analysis of the proportion of fluorescence intensity in layer VI versus layer V supported our observations (Fig. 6B). Together, our electroporation experiments show that overexpression of Tubb2b-E421K perturbs the accuracy of target innervation by both local and long-range projections, processes that normally proceed through the generation of interstitial branches (27,28).

TUBB2B-E421K heterodimers co-assemble into microtubule networks

The dominant axonal phenotypes associated with TUBB2B-E421K could occur through various mechanisms. The E421K mutation could block the chaperone-mediated tubulin folding pathway and lead to globally decreased levels of tubulin heterodimer formation, as reported for other *TUBB2B* mutations (10). Alternatively, folded mutant αβ-heterodimers could incorporate into and alter microtubule polymer function, as reported for *TUBB3* mutations that cause CFEOM (11).

To explore these possibilities, we first tested the efficiency of TUBB2B-E421K αβ-heterodimer formation *in vitro*. We generated wild-type (TUBB2B-WT-V5) and mutant (TUBB2B-E421K-V5) TUBB2B expression constructs fused to the C-terminal V5 epitope tag and performed *in vitro* transcription and translation in reticulocyte lysates, a cell-free system containing the chaperones necessary to mediate tubulin folding. Additionally, we expressed two mutants, TUBB2B-S172P-V5 and TUBB2B-F265L-V5, previously shown to obstruct the tubulin folding process (10). TUBB2B-WT-V5, TUBB2B-S172P-V5 and TUBB2B-F265L-V5 cDNAs were transcribed and translated at equivalent levels, while the production of TUBB2B-E421K-V5 was somewhat reduced, even in the presence of protease inhibitors (Supplementary Material, Fig. S8), indicating *TUBB2B-E421K* is transcribed and/or translated inefficiently. For αβ-heterodimer formation and cycling assays, the production level of TUBB2B-E421K-V5 polypeptide was adjusted by increasing the concentration of template cDNA to match the WT output levels (Fig. 7A). Electrophoresis under native conditions revealed that while production of native TUBB2B-E421K-V5 αβ-heterodimer was decreased compared with that of TUBB2B-WT-V5, it was greater than S172P and F265L αβ-heterodimer production (Fig. 7B).

To assess whether folded E421K αβ-heterodimers could assemble into microtubule polymers, the TUBB2B-WT-V5 and TUBB2B-E421K-V5 αβ-heterodimers formed in reticulocyte lysates were co-polymerized with native brain tubulin. The efficiency of TUBB2B-E421K-V5 incorporation into the polymer lattice, scored by one round of microtubule polymerization and depolymerization, was similar, though slightly reduced, when compared with the level of TUBB2B-WT-V5 incorporation (Fig. 7C). We evaluated the co-polymerization of TUBB2B-E421K *in vivo* by transfecting HeLa cells with *TUBB2B-WT-V5* or *TUBB2B-E421K-V5* expression constructs, and extracting soluble tubulin with methanol fixation. Consistent with the *in vitro* polymerization assay, immunostaining against TUBB2B-WT-V5 and TUBB2B-E421K-V5 revealed comparable levels of E421K and WT TUBB2B incorporation into the microtubule lattice, when adjusted for total V5 expression (Fig. 7D). Thus, although the E421K substitution reduces the efficiency of αβ-heterodimer formation, the successfully folded polypeptide assembles into microtubule structures both *in vitro* and *in vivo* at levels that are quantitatively similar to those of TUBB2B-WT αβ-heterodimers.

Downloaded from http://hmg.oxfordjournals.org/ at Serials Department on January 4, 2013

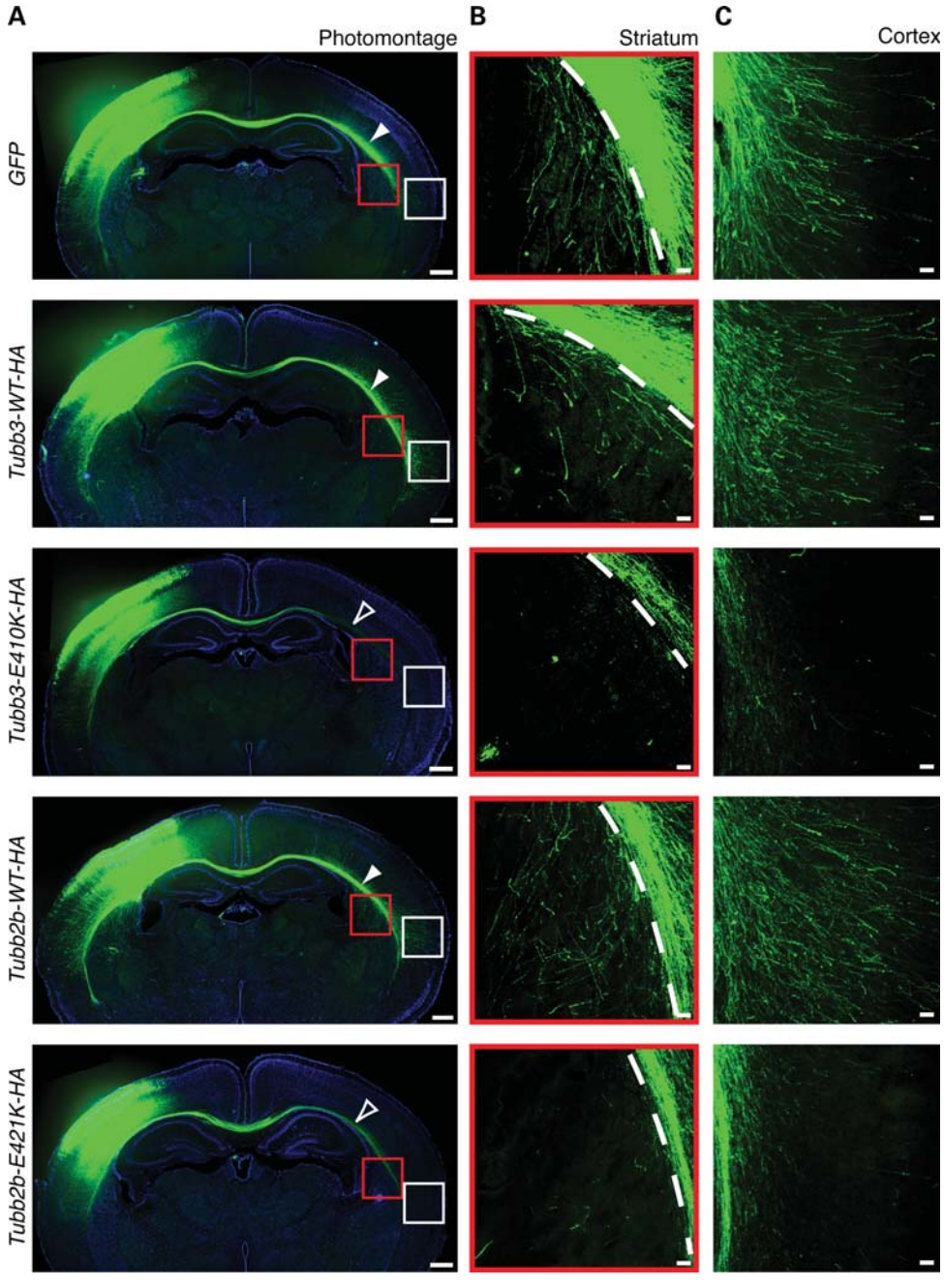

Figure 5. Tubb2b-E421K-HA perturbs CPN terminal axon extension. Fluorescent micrographs of mouse CPN electroporated at E15.5 and analyzed at P6. (**A**) Photomontage of coronal sections at P6 shows distal thinning of CPN fibers in brains electroporated with *Tubb3-E410K-HA* and *Tubb2b-E421K-HA* (open white arrowheads) compared with GFP and WT controls (solid white arrowheads). Some mutant axons do reach the most lateral region of the CC. (**B** and **C**) High magnification microscopy shows that CPN expressing GFP, Tubb3-WT-HA or Tubb2b-WT-HA send interstitial branches into the contralateral striatum (B, red boxes from A) and contralateral neocortex (C, white boxes from A), whereas CPN expressing Tubb3-E410K-HA and Tubb2b-E421K-HA fail to do so. $n = 4$ (GFP), $n = 3$ (Tubb3-WT-HA), $n = 6$ (Tubb3-E410K-HA), $n = 5$ (Tubb2b-WT-HA), $n = 5$ (Tubb2b-E421K-HA). Each n represents one embryo. CPN, callosal projection neurons; CC, corpus callosum. Scale bars: 400 μm (A), 50 μm (B and C).

β-Tubulin E421K substitution alters microtubule dynamics *in vivo*

To investigate how E421K heterodimers alter microtubule function, we utilized budding yeast, which provides several advantages for exploring the functional consequences of human tubulin mutations. First, yeast permits the rapid insertion of site-directed mutations at the endogenous tubulin locus under the native promoter and regulatory elements. Such mutations can then be combined with fluorescently

Downloaded from http://hmg.oxfordjournals.org/ at Serials Department on January 4, 2013

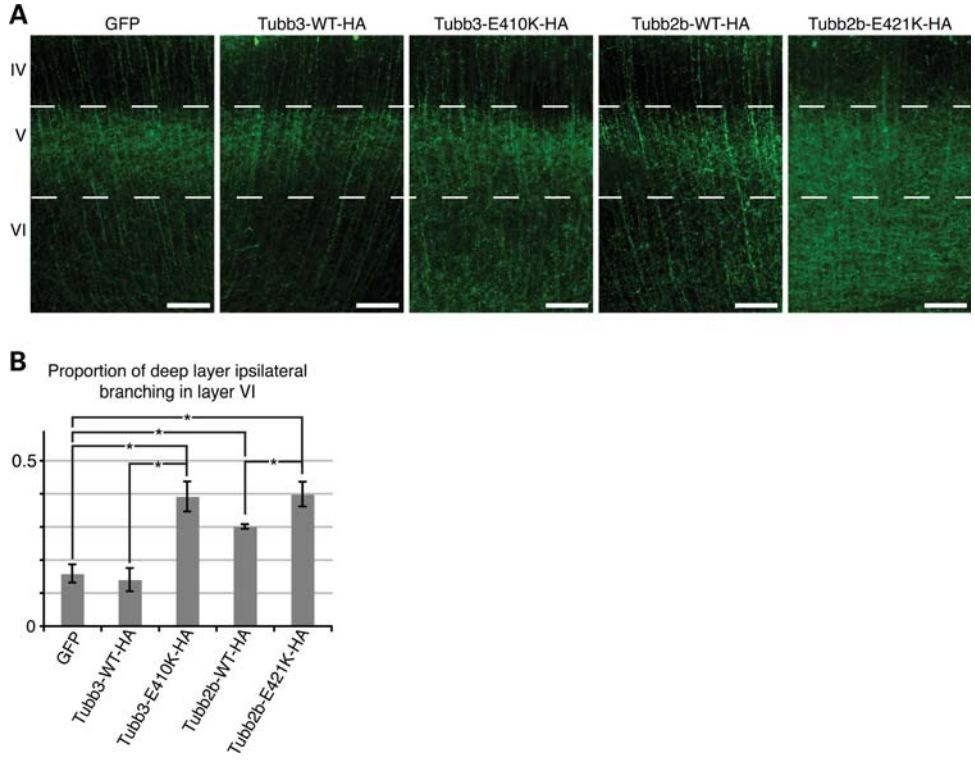

Figure 6. Tubb2b-E421K-HA alters the layer specificity of local branching. Fluorescent micrographs of CPN electroporated at E15.5 and analyzed at P6. (**A**) Axons of CPN expressing GFP, Tubb3-WT-HA, or Tubb2b-WT-HA have sent dense interstitial branches into layer V of the ipsilateral cortex, but few branches into the deeper layer VI. In contrast, axons of CPN expressing Tubb3-E410K-HA and Tubb2b-E421K-HA do not show similar specificity as a high density of branching is seen in layer VI, in addition to layer V. (**B**) Quantitative analysis of the fluorescence intensity in the deep layers (V and VI) reveals that 0.16 ± 0.03 of GFP, 0.14 ± 0.04 of Tubb3-WT-HA and 0.30 ± 0.01 of Tubb2b-WT-HA branches target layer VI. *Tubb2b-WT-HA* electroporation significantly increases the proportion of layer VI branching ($P < 0.01$ compared with GFP). There is, however, also a significant increase in the proportion of branching in layer VI in both mutant conditions, with 0.39 ± 0.05 of Tubb3-E410K-HA ($P < 0.01$ compared to Tubb3-WT-HA control) and 0.40 ± 0.04 of Tubb2b-E421K-HA ($P < 0.05$ compared with Tubb2b-WT-HA control) branching in layer VI. $n = 4$ (GFP), $n = 3$ (Tubb3-WT-HA), $n = 3$ (Tubb3-E410K-HA), $n = 5$ (Tubb2b-WT-HA), $n = 4$ (Tubb2b-E421K-HA). Each n represents one embryo. One-way ANOVA with the *post hoc* Tukey *t*-test was used for multiple comparisons. IV, neocortical layer IV; V, neocortical layer V; VI, neocortical layer VI. Error bars represent SEM. $^*P < 0.05$. Scale bars: 100 μm.

tagged cytoskeletal proteins. This allows for phenotypic examination at a level of experimental control not easily attained in other systems, in which transgenic or over-expression approaches can result in non-physiological paradigms. Second, individual fluorescently tagged yeast microtubules and kinesin motors are easily discerned during time-lapse microscopy, which allows one to quantitatively assess parameters of microtubule dynamics and kinesin localization. Third, CFEOM-causing mutations have now been identified in multiple β-tubulin isotypes, each of which has a different level and pattern of expression. Yeast has a single β-tubulin isotype (Tub2p), which shares high sequence conservation with mammalian β-tubulin isotypes (Fig. 2C). Thus, modeling disease-causing mutations in yeast helps control for these differences and should ultimately help to discriminate between residue-specific and isotype-specific phenotypes.

For these reasons, we introduced the E421K corresponding mutation into budding yeast. Heterozygous diploids were recovered at the expected frequency and displayed no growth defects when cultured in nutrient-rich media, while haploid *tub2-E410K* and *tub2-E421K* spores were inviable, demonstrating compromised microtubule function (Supplementary Material, Fig. S9). Since CFEOM-causing substitutions in TUBB3 compromise microtubule dynamics (11), we grew diploid *tub2-E421K* heterozygous cells on media containing increasing concentrations of the microtubule-destabilizing drug carbendazim to assay for changes in microtubule stability. Compared with the WT strain, the *tub2-E421K* strain showed an increased resistance to carbendazim (Fig. 8A and B). Thus the E421K substitution, similar to E410K and other CFEOM-causing substitutions (11), stabilizes microtubules *in vivo*. In contrast, Tub2p haploinsufficiency substantially increased carbendazim sensitivity (Fig. 8A and B). Importantly, these results demonstrate that E421K does not result in a loss of function in yeast, and affects microtubule dynamics in a dominant manner.

To determine how E421K alters microtubule stability, we generated WT and mutant β-tubulin strains expressing GFP-α-tubulin (*GFP-TUB1*) and used time-lapse microscopy to observe the dynamic behavior of astral microtubules in G1 cells (Supplementary Material, Movie S1). Astral microtubules in cells harboring the E421K substitution spent less time in the attenuated state and had significantly increased rates of polymerization and depolymerization when compared

Downloaded from http://hmg.oxfordjournals.org/ at Serials Department on January 4, 2013

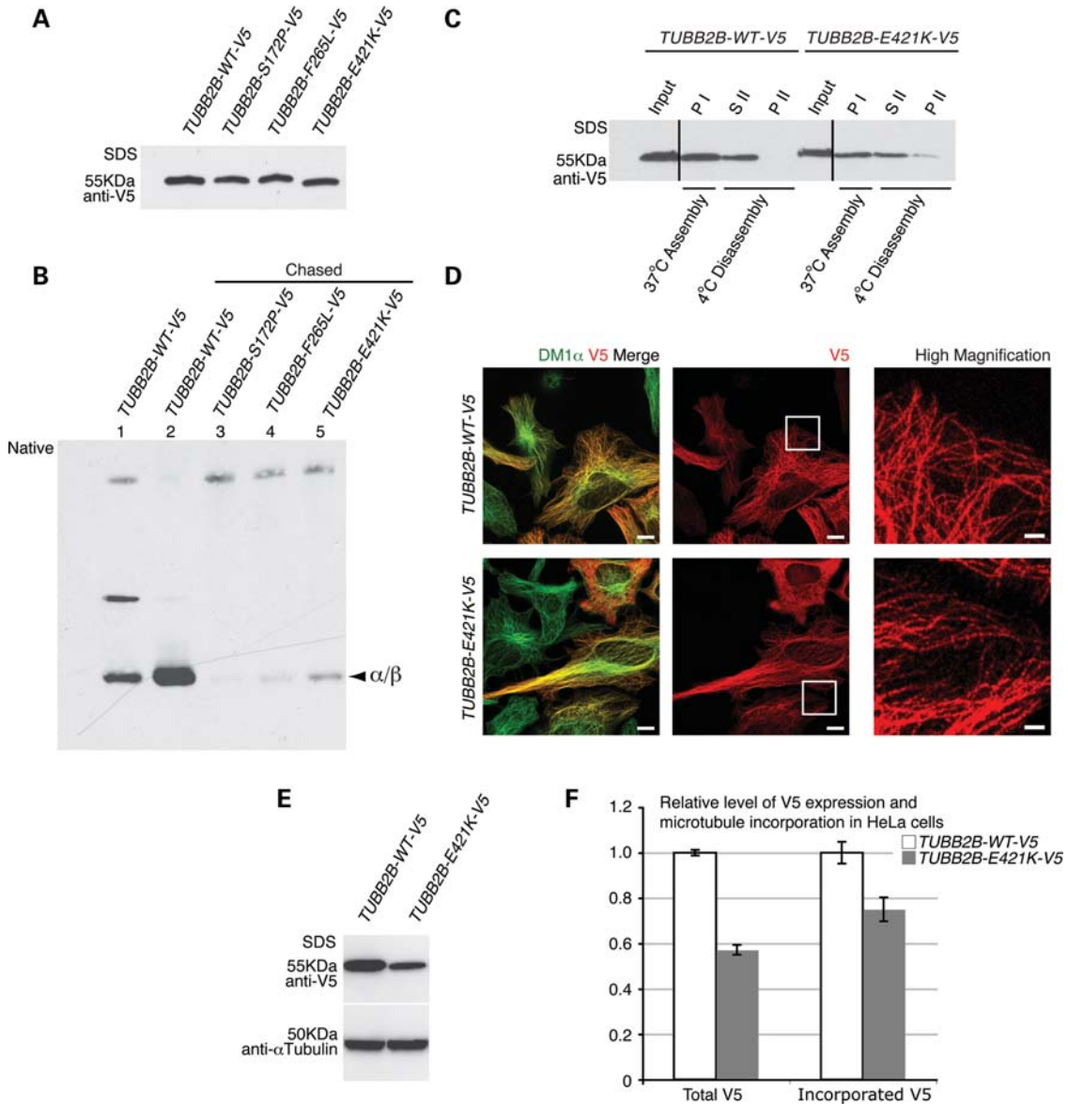

Figure 7. The E421K substitution decreases the efficiency of αβ-heterodimer formation, but permits incorporation into microtubule polymers. TUBB2B-E421K-V5 αβ-heterodimer formation and incorporation were assayed by *in vitro* transcription and translation using rabbit reticulocyte lysates and *in vivo* by HeLa cell transfection. (**A**) WT and mutant TUBB2B-V5 plasmids show equivalent polypeptide production *in vitro* after DNA adjustment. (**B**) *In vitro* formation of WT and mutant TUBB2B αβ-heterodimers analyzed by native gel electrophoresis. Chasing the reaction with purified porcine tubulin releases newly synthesized subunits from folding machinery (compare α/β bands from lane 2 to lane 1). The E421K substitution leads to decreased αβ-heterodimer formation (lane 5) compared with WT (lane 2), and greater formation than S172P (lane 3) and F265L (lane 4). (**C**) *In vitro* microtubule polymerization of porcine brain tubulin and V5-tagged heterodimers. WT and E421K TUBB2B αβ-heterodimers co-polymerize with brain tubulin at comparable efficiencies. Microtubules containing WT and E421K αβ-heterodimers are cold-labile (compare SII with PI), although some insoluble E421K heterodimer remains after cold disassembly (PII). The efficiency of microtubule incorporation of TUBB2B-E421K-V5 αβ-heterodimers was 90 ± 17% relative to WT (mean ± SEM, $n = 3$, $P > 0.05$). PI, pellet following assembly; SII, soluble protein following cold-induced disassembly; PII, insoluble protein following cold-induced disassembly. Vertical lines denote the removal of irrelevant lanes. (**D**) Exogenously expressed TUBB2B-E421K-V5 (V5, red) co-localizes with α-tubulin (Dm1α, green), and has a filamentous appearance (high magnification, boxed regions), similar to TUBB2B-WT-V5, demonstrating efficient assembly with HeLa cell microtubules. (**E**) Quantitative western blot of total protein expression demonstrates lower amounts of mutant TUBB2B compared with WT. (**F**) Fluorescence analysis, after soluble protein extraction, demonstrates roughly equivalent efficiencies of incorporation between WT and mutant proteins, when adjusted for total protein expression in (E). Total TUBB2B-E421K-V5 protein expression is reduced by 43% compared with WT (WT = 1.0 ± 0.01, E421K = 0.57 ± 0.02, $P < 0.0001$; $n = 3$, $n =$ one transfected culture), while the amount of incorporated TUBB2B-E421K-V5 protein is reduced by 25% (WT = 1.0 ± 0.05, E421K = 0.75 ± 0.05, $P < 0.0005$; $n = 111$ WT and 92 E421K, $n =$ one cell). Scale bars: 10 μm (×63; left and middle panels), 2 μm (×100; high magnification, right panel).

with microtubules in WT cells. However, the time that individual E421K microtubules spent growing and shortening remained largely unaffected (Fig. 8C and D). Thus, the E421K substitution alters specific aspects of microtubule dynamic instability in a manner that may increase overall polymer stability.

Downloaded from http://hmg.oxfordjournals.org/ at Serials Department on January 4, 2013

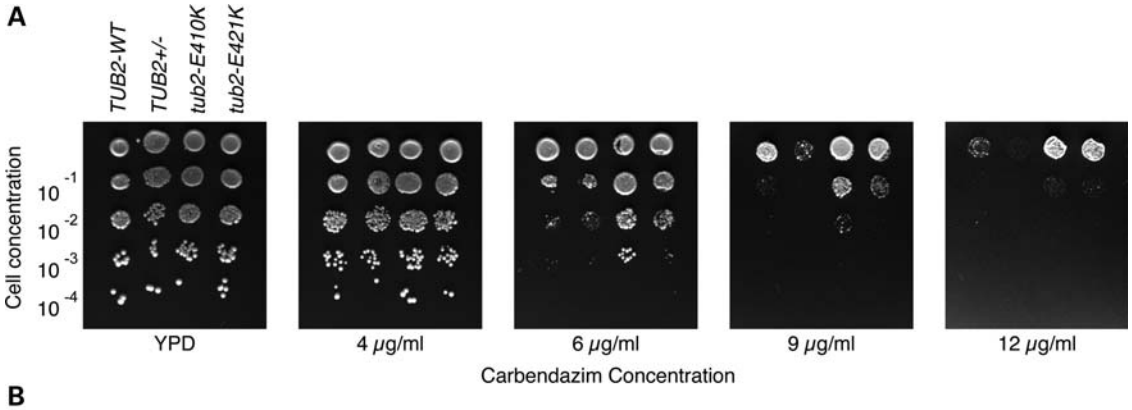

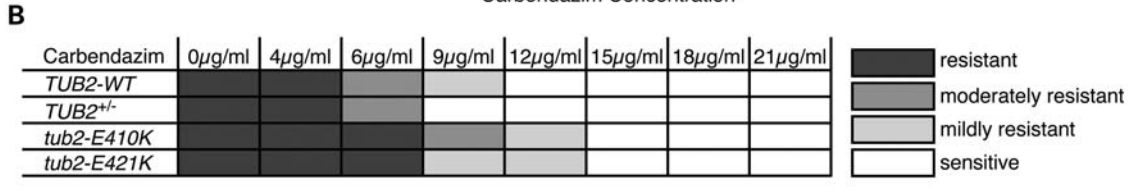

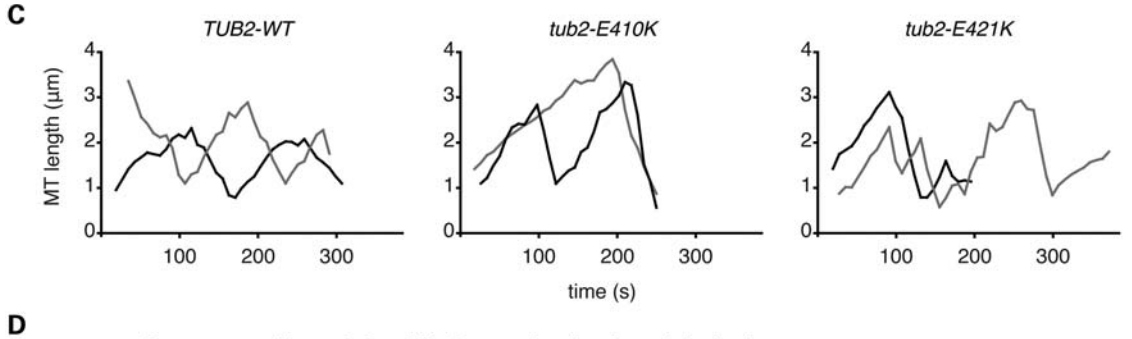

D

Parameters of dynamic instability for cytoplasmic microtubules in vivo.

	TUB2-WT	*tub2-E410K*	*tub2-E421K*
Number of cells/microtubules analyzed	10 / 22	7 / 20	13 / 32
Mean polymerization rate (μm/min)	1.35 ± 0.31	1.09 ± 0.27 **	1.60 ± 0.42 *
Mean depolymerization rate (μm/min)	2.02 ± 0.66	3.35 ± 1.09 **	3.17 ± 1.07 **
Catastrophe frequency (min^{-1})	0.62 (21)	0.45 (21)	0.91 (28)
Rescue frequency (min^{-1})	0.46 (9)	0.32 (5)	0.51 (10)
Time spent polymerizing (%)	47	67	54
Time spent depolymerizing (%)	37	25	39
Time spent attenuated (%)	17	9	7
Mean growth duration (s)	55 (27)	92 (27) **	49 (33)
Mean shortening duration (s)	42 (28)	40 (23)	33 (36) *
Mean attenuated duration (s)	36 (15)	35 (9)	36 (6)

Sample number shown in parenthesis; Error = SD; *p < 0.05; **p < 0.005 versus WT by unpaired, two-tailed t-test.

Figure 8. The E421K substitution alters microtubule dynamics. (**A**) A representative carbendazim sensitivity assay. Diploid cells were serially diluted and plated on rich YPD media containing increasing concentrations of carbendazim, a microtubule destabilizing agent. The Tub2p haploinsufficient cells ($TUB2^{+/-}$) were super-sensitive to carbendazim. In contrast, both heterozygous *tub2-E410K* and heterozygous *tub2-E421K* cells displayed increased resistance to carbendazim compared with WT cells. (**B**) Chart depicting a summary of more than three independent carbendazim assays with concentration ranging from 0 –21 μg/ml. Shaded boxes depict the degree of carbendazim resistance. (**C**) Life-time history plots of two representative individual microtubules from diploid WT (left), heterozygous *tub2-E410K* (center) or heterozygous *tub2-E421K* (right) cells in G1. (**D**) Parameters of dynamic instability determined for each strain. Notably, *tub2-E421K* microtubules show increased rates of polymerization, depolymerization, and reduced time spent in attenuation. Error given as standard deviation. Number of events is in parentheses. MT, microtubule. $^{*}P < 0.05$, $^{**}P < 0.005$ versus WT by unpaired Student's *t*-test.

The E421K substitution in β-tubulin can disrupt kinesin–microtubule interactions in yeast

Yeast cells with tub2p-E421K exhibited altered microtubule dynamics, including faster depolymerization rates that are reminiscent of cells lacking Kip3p, a plus-end-directed motor protein that regulates microtubule dynamics (29,30). Furthermore, E421 has previously been shown to be critical for kinesin–microtubule interactions *in vitro* (23,24). We therefore examined whether the E421K substitution affects

Downloaded from http://hmg.oxfordjournals.org/ at Serials Department on January 4, 2013

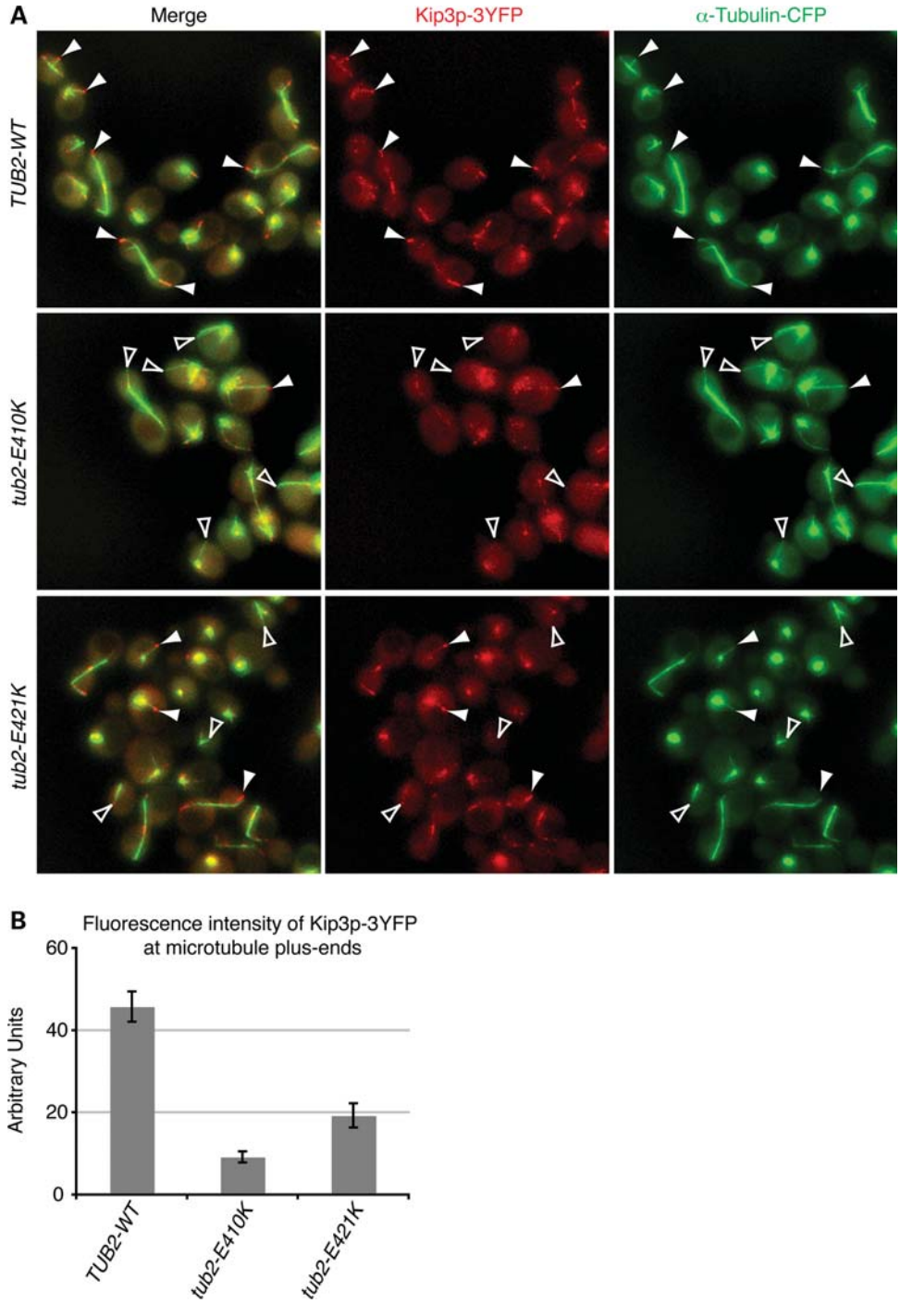

Figure 9. E421K reduces the localization of kinesin Kip3p at microtubule plus-ends. (**A**) Representative Z-series maximum projections showing fluorescently labeled Kip3p (red) and α-tubulin (green) in live diploid WT, heterozygous *tub2-E410K* and heterozygous *tub2-E421K* yeast cells. Kip3p-3YFP forms bright foci at the plus-ends of most WT astral microtubules, but these bright foci are rarely found at the plus-ends of mutant astral microtubules (solid white arrowheads). Similar to microtubules in *tub2-E410K* cells, most astral microtubule plus-ends in *tub2-E421K* cells had a significant reduction in Kip3p-3YFP localization (open white arrowheads). Signal intensities were adjusted equally in both channels for all strains. (**B**) Quantification of Kip3p-3YFP levels at the plus-ends of microtubules in cells containing Tub2, tub2p-E410K and tub2p-E421K. Localization of Kip3p intensity was reduced by 58% in *tub2-E421K* cells and by 81% in *tub2-E410K* cells. 60–150 microtubules from three to four clones on two separate days each were imaged for each condition. $n \geq 6$ for all conditions. *n* represents the averaged values for each clone from 1 day. Error represented as SEM in graphs. $P < 0.001$ versus WT by unpaired Student's *t*-test.

Kip3p localization *in vivo* by generating WT and heterozygous mutant cells that co-express equivalent amounts of Kip3p fused to three tandem copies of YFP (Kip3p-3YFP) (Supplementary Material, Fig. S10). In WT cells, Kip3p-3YFP formed bright foci at the plus ends of growing microtubules and lower intensity spots along the microtubule lattice (Fig. 9A. Compared with WT signal, Kip3p-3YFP signal intensity was significantly reduced on the tips of E421K

Downloaded from http://hmg.oxfordjournals.org/ at Serials Department on January 4, 2013

harboring microtubules, and severely reduced on the tips of E410K harboring microtubules (Fig. 9A). Quantitative analysis of foci intensity supported our observations (Fig. 9B). We next generated WT and heterozygous mutant cells that co-express equivalent amounts of another yeast cytoplasmic kinesin, Kip2p, fused to three tandem copies of YFP (Kip2p-3YFP). We found that Kip2p-3YFP localization was not significantly reduced on microtubule plus-ends harboring the E421K substitution (Supplementary Material, Fig. S11).

Since Kip3p is a microtubule depolymerase (29,30), it is possible that microtubule stabilization by E421K results in its diminished localization. To address this question, we measured Kip3p localization in cells harboring the C354S substitution, previously shown to directly stabilize microtubules both *in vivo* and *in vitro* (31). In contrast to E421K and E410K, the C354S substitution produced a nearly 3-fold increase in Kip3p-3YFP localization at the microtubule tips (Supplementary Material, Fig. S12). Thus, reduced Kip3p-3YFP localization on E421K microtubules is not a result of increased microtubule stability. Together, our data show that E421K can alter kinesin localization and microtubule dynamics in a dominant manner and result in axonal dysinnervation in both central and peripheral axon tracts.

DISCUSSION

We have determined that a heterozygous TUBB2B-E421K amino acid substitution underlies a syndrome characterized by CFEOM and intellectual disability. Using MRI with DTI, we found underlying PMG, asymmetric basal ganglia dysmorphisms and a paucity of homotopic connections. Overexpression of TUBB2B-E421K in mouse CPN prevents normal development of homotopic connectivity and target innervation, without perturbing cell migration. Yeast microtubules harboring the E421K substitution had increased polymerization and depolymerization rates, and reduced localization of Kip3p at their plus ends. Together, these data demonstrate that mutations in *TUBB2B* can induce axonal dysinnervation as a primary phenotype, and provide further insight into the genetic, molecular and cellular basis underlying the spectrum of tubulin-related neurological phenotypes.

Tubb2b dysfunction and axonal dysinnervation

Two major themes regarding axon development emerge from our studies. First is the apparent primacy of axonal dysinnervation in a *TUBB2B* disorder. All previously identified *TUBB2B* mutations result in severe cortical dysplasia (10,12,14), raising the possibility that associated white matter abnormalities are secondary phenotypes. Here, we present several lines of evidence that support TUBB2B-E421K is a cause of primary axonal dysinnervation. First, all three affected family members have CFEOM, of which all dominant forms are known to result from primary axonal dysinnervation (11,32). Second, DTI analysis showed that the affected daughters developed an aberrant pattern of commissural fiber trajectories that is not common for other PMG patients we examined. Third, we demonstrated by electroporation that Tubb2b-E421K can induce axonal dysinnervation with no discernable neuronal production or migratory defects. Finally, introduction of E421K into yeast β-tubulin produced molecular phenotypes that resemble the effects of E410K, a substitution in TUBB3 known to cause primary axonal dysinnervation.

The second emergent theme is the developmental selectivity of Tubb2b-E421K associated phenotypes. Overexpression of Tubb2b-E421K does not inhibit CPN axons from crossing the midline, but does disrupt their development as they traverse past the midline. Moreover, despite relatively normal growth of the primary axon, E421K-expressing neurons fail to generate interstitial branches appropriately; they send promiscuous branches into layer VI of the ipsilateral cortex, whereas their axons fail to innervate contralateral target regions. Both of these processes proceed through the development of interstitial branches (27,28). One explanation for these observed phenotypes is that E421K selectively alters a restricted set of molecular pathways associated with post-midline guidance, such as Wnt5a or calcium-dependent kinase 1α signaling (33–37). Since many neurological disorders are associated with selective phenotypes despite mutations in broadly expressed genes, understanding the relationship between Tubb2b-E421K and the selective vulnerability of certain developmental events and/or cell types is a broadly important and clinically significant area of investigation.

Dominant and potentially haploinsufficient contributions of TUBB2B-E421K

In agreement with previous reports (11,32), our findings support a dominant etiology for CFEOM. Genetically, CFEOM segregates with the E421K substitution, but not with most other reported TUBB2B substitutions. Functionally, yeast expressing the *tub2-E421K* allele have increased microtubule stability, the phenotypic opposite of yeast haploinsufficient for the *TUB2* allele. Furthermore, overexpression of Tubb2b-E421K in wild-type CPN recapitulates human axonal phenotypes.

It remains less clear whether *TUBB2B* mutations cause PMG through dominant or haploinsufficient effects. Previous functional studies support neuronal *TUBB2B* haploinsufficiency because mutant proteins fold and incorporate poorly. Furthermore, knockdown of *Tubb2b* in rat cortical neurons induces a migratory defect (10), providing a strong link between *TUBB2B* haploinsufficiency and PMG. We show that the E421K substitution reduces TUBB2B αβ-heterodimer production, while it does not significantly alter polymer incorporation. Thus, E421K may cause PMG as a result of TUBB2B haploinsufficiency. *TUBB2B* is expressed, however, by both post-mitotic neurons and mitotic progenitors, including radial glia (38). Radial glia guide cortical neuron migration (39–45) and their maldevelopment are associated with PMG (46–48). Thus, an alternative possibility is that *TUBB2B*-related PMG is the result of defective radial glia, in which microtubule function is dominantly altered. Neuropathological analysis of a fetus that harbored the TUBB2B-S172P substitution showed that radial glia were disorganized and lacked apical–basal orientation (10,19). Furthermore, kinesin-binding site substitutions D417N and E421K in TUBB2B, which is expressed in radial glia, cause PMG, while kinesin-binding site substitutions D417N/H and E410K in TUBB3, which is not expressed in

Downloaded from http://hmg.oxfordjournals.org/ at Serials Department on January 4, 2013

radial glia, do not cause PMG (11,12). Thus far, all functional studies of *TUBB2B* mutations have used electroporation to model the human phenotypes, and radial glial phenotypes are not easily discerned by this approach (49). The generation of knock-in animal models harboring *Tubb2b* disease mutations will help resolve the cell type and molecular etiology of this phenotype.

Differences between TUBB2B-CFEOM and TUBB3-CFEOM syndromes

There are apparent differences between CFEOM-causing mutations in β-tubulin isotypes *TUBB2B* and *TUBB3*. First, the frequency of CFEOM-causing mutations appears to be much higher in *TUBB3* than in *TUBB2B*. We have reported 29 CFEOM probands with *TUBB3* mutations (11), but only one with a *TUBB2B* mutation. Second, the lone *TUBB2B* mutation in our CCDD cohort associates with PMG, whereas *TUBB3* mutations do not cause cortical malformations, but can associate with additional cranial nerve dysfunction, progressive axonal polyneuropathy and central white matter tract abnormalities (11).

These apparent differences may result from distinct spatiotemporal expression patterns of *TUBB2B* and *TUBB3*. The expression of *TUBB2B,* but not *TUBB3,* in mitotic progenitors, including radial glia (4,38,50), may account for the uniform prevalence of PMG associated with *TUBB2B* but not *TUBB3* mutations. Still, mutations in *TUBB3* can sometimes result in cortical malformations, and even PMG, though these mutations do not simultaneously cause CFEOM (13). Thus these mutations may be mechanistically different than CFEOM-causing mutations in *TUBB2B* and *TUBB3*. Isotype expression differences may also render *TUBB2B* mutations to be generally more deleterious than *TUBB3* mutations, leading to a higher incidence of embryonic lethality and a paucity of *TUBB2B* mutations in our CFEOM cohort. In support of this, 6 of the 14 *TUBB3* mutations have been familial (11,13), while this is the first of nine reported *TUBB2B* mutations to be so. Finally, the association of TUBB3-D417N/H and -E410K substitutions with peripheral sensorimotor axonal polyneuropathy may reflect the persistently elevated expression of *TUBB3*, but not *TUBB2B*, in the peripheral nervous system (51).

TUBB2B-CFEOM and TUBB3-CFEOM phenotypes may also differ due to intrinsic differences in isotype function. Though β-tubulin isotypes show over 90% conservation in amino acid sequence, key differences exist, especially in the C-terminal tail (3,52) which is known to differentially regulate MAP binding (53–56). Microtubules with different isotype compositions also exhibit different dynamic profiles (57). Interestingly, it was recently reported that a *de novo* D417N substitution in TUBB2B resulted in symmetric PMG, but not CFEOM (12). This finding might suggest that the conserved D417 residue has divergent functions in distinct isotypes. However, the TUBB3-D417N substitution results in a relatively mild phenotype in which both CFEOM and a progressive axonal neuropathy have variable expressivity (11). Thus, additional individuals with TUBB2B-D417N substitutions will need to be identified in order to determine whether this substitution can also result in CFEOM.

Molecular phenotypes and CFEOM pathogenesis

By defining an allelic series of CFEOM-causing mutations in *TUBB3* and now *TUBB2B*, strong correlations emerge between molecular phenotypes and the disease. All nine CFEOM mutations in our cohort, from two different human isotypes, produce resistance to the microtubule destabilizing drug carbendazim, or its precursor benomyl, and all alter the dynamic growth and shortening of microtubules. This is especially striking since alanine-scanning analysis of yeast Tub1p only produced 6 of 53 mutations that confer any resistance to benomyl, whereas 37 mutations resulted in benomyl sensitivity (58). If microtubule dynamics were not related to CFEOM pathogenesis, it is unlikely that 100% of CFEOM mutations would produce benomyl resistance. Thus, our studies currently support a model in which altered microtubule dynamics underlie cranial nerve misguidance.

Structurally, CFEOM-causing substitutions alter residues predicted to directly interact with MAP and motor proteins, or reside in regions at the interface between αβ-heterodimers (11,14,15). In theory, these substitutions could alter microtubule dynamics by directly interfering with tubulin–tubulin interactions, or by changing the activity of proteins that regulate the growth and shortening of microtubules, such as kinesins (59). Previous analysis of cytoplasmic kinesins in the yeast model system revealed that five of eight CFEOM mutations in *TUBB3* perturbed the normal localization of the regulatory kinesin Kip3p, which depolymerizes microtubule plus ends (29,30), whereas Kip2p localization was less severely affected. This trend suggests that some CFEOM mutations alter regulatory molecules, thus leading to pathogenic microtubule dynamics. In this study, we model a CFEOM mutation from a second human tubulin isotype, *TUBB2B*, and again find that Kip3p localization is more severely affected than that of Kip2p. The striking consistency of molecular phenotypes among CFEOM mutations argues that the emergent biochemical properties are central to the molecular etiology of CFEOM. Future *in vitro* biophysical and biochemical studies, combined with *in vivo* modeling in neurons will be necessary to determine the precise molecular cascades that lead to cranial nerve misguidance. These studies will also likely provide important insights into the role of individual β-tubulin isotypes and specific residues during normal development.

MATERIALS AND METHODS

Detailed methods can be found in the Supplementary Methods available online.

Clinical and genetic studies

A family with inherited CFEOM and PMG was enrolled in an ongoing genetic study of CCDD. The study was conducted according to Declaration of Helsinki principles, approved by the Boston Children's Hospital Institutional Review Board, and written informed consent was obtained from each participant and/or his or her guardian. Participants underwent medical examinations and/or provided medical records.

Downloaded from http://hmg.oxfordjournals.org/ at Serials Department on January 4, 2013

Linkage and mutation analysis were performed as previously described (11,17).

Magnetic resonance imaging

Diagnostic structural (I:2, II:2, II:3) and diffusion (II:2, II:3) MRI scans were reviewed. A structural and diffusion MRI of an age-matched female control was acquired at Boston Children's Hospital following appropriate Institutional Review Board approval and informed consent. CC fibers were segmented from DTI data using the Diffusion Toolkit developed at the Athinoula A. Martinos Center for Biomedical Imaging, Department of Radiology, Massachusetts General Hospital (Ruopeng Wang, Van J. Wedeen, TrackVis.org; http://trackvis.org). The color coding of fibers is based on a standard RGB code (red: left–right; green: front–back; blue: superior–inferior).

In utero electroporation and histology

All animal experiments were carried out in accordance with protocols approved by the Boston Children's Hospital Institutional Animal Care and Use Committee and with institutional and federal guidelines. Electroporation, histology and immunocytochemistry were performed as previously described (60–62). Briefly, DNA (1 mg/ml for each plasmid) was pressure injected into the lateral ventricle of embryos of timed pregnant CD1 females, and five 50 ms 45 mV pulses at 1 s intervals were applied. Brains were fixed at appropriate ages and cut into 50 μm sections. Primary antibody was applied overnight at 4°C and secondary antibody was applied for 3 h at room temperature the next day.

Immunofluorescence analysis

Midline crossing was quantified as the ratio of contralateral to ipsilateral axonal GFP intensity in the CC. Ipsilateral interstitial branching was quantified the ratio of layer VI to layer V branching. Image intensities were acquired using ImageJ software (NIH), and corrected for background intensity.

In vitro heterodimer formation and cycling

The cDNA encoding human *TUBB2B* was subcloned into pcDNA3.2/V5 DEST (Invitrogen), and disease-associated mutations were introduced using site-directed mutagenesis (Agilent Technologies). 125 ng of WT, S172P and F265L, and 188.5ng of E421K plasmid DNA were incubated with 25 μl of reticulocyte lysate, with or without protease inhibitors (Roche) for heterodimer folding and cycling assays. All subsequent steps were performed as previously described (11). Briefly, following a 90-min incubation at 30°C, samples were chased with purified porcine tubulin, $MgCl_2$ and GTP, and a small aliquot was analyzed by native PAGE. The remaining sample was cycled with porcine tubulin, and analyzed by SDS–PAGE. The relative cycling efficiency of mutant tubulin was quantified using the ImageJ densitometry software and normalized against the WT.

HeLa cell incorporation assay

Transfected HeLa cells were fixed with methanol to extract soluble tubulin, and stained with fluorescent antibodies, as previously described (11). Total V5 expression was determined by collecting total protein lysate and analyzing by standard western blotting procedures, and levels of V5 incorporation were determined by quantitative immunofluorescence of average pixel intensity per cell.

Yeast strains

Mutant yeast strains harboring *tub2* mutations corresponding to human *TUBB2B* and *TUBB3* CFEOM mutations, and expressing GFP-Tub1 or CFP-Tub1 and Kip3p-3YFP or Kip2p-3YFP were generated as previously described (11,29,63).

Microtubule stability assay

WT and mutant *tub2* yeast strains were grown on increasing concentrations of carbendazim and scored for resistance, as previously described (11).

Yeast *in vivo* microtubule dynamics

Microtubules were visualized *in vivo* by time-lapse imaging of WT and mutant *tub2* strains expressing GFP-Tub1, as previously described (11).

Kip3p and Kip2p plus-end localization

Localization of Kip3p-3YFP or Kip2p-3YFP to plus ends of astral microtubules was assessed in WT and mutant *tub2* strains expressing CFP-Tub1p and Kip3p-3YFP or Kip2p-3YFP using live cell confocal microscopy as previously described (11,29).

SUPPLEMENTARY MATERIAL

Supplementary Material is available at *HMG* online.

ACKNOWLEDGEMENTS

The authors would like to thank the study participants for their generosity and time, Kathryn North, Steve Vuvic, Jennifer Lorenzo and Nathalie Pride for providing clinical data, Kiho Im and Michael Paladino for providing MRI data, Matt Gregas for statistical consultation, Carlos Lois for critical reagents and members of the Engle Lab for critical reading of the manuscript.

Conflict of Interest statement. None declared.

FUNDING

Supported by NIH R01EY12498 and IDDRC HD018655 (E.C.E.) and by NIH R01GM094313 and Research Grant No. 5-FY12-80 from the March of Dimes Foundation (M.L.G.). S.C. is funded by the HHMI Medical Fellowship

Downloaded from http://hmg.oxfordjournals.org/ at Serials Department on January 4, 2013

and Harvard Medical School. E.C.E. is a Howard Hughes Medical Institute Investigator.

REFERENCES

1. Little, M. and Seehaus, T. (1988) Comparative analysis of tubulin sequences. *Comp. Biochem. Physiol. B.*, **90**, 655–670.
2. Luduena, R.F. (1993) Are tubulin isotypes functionally significant. *Mol. Biol. Cell.*, **4**, 445–457.
3. Sullivan, K.F. and Cleveland, D.W. (1986) Identification of conserved isotype-defining variable region sequences for four vertebrate beta tubulin polypeptide classes. *PNAS.*, **83**, 4327–4331.
4. Sullivan, K.F., Havercroft, J.C., Machlin, P.S. and Cleveland, D.W. (1986) Sequence and expression of the chicken beta 5- and beta 4-tubulin genes define a pair of divergent beta-tubulins with complementary patterns of expression. *Mol. Cell Biol.*, **6**, 4409–4418.
5. Kaltschmidt, B., Glatzer, K.H., Michiels, F., Leiss, D. and Renkawitz-Pohl, R. (1991) During Drosophila spermatogenesis beta 1, beta 2 and beta 3 tubulin isotypes are cell-type specifically expressed but have the potential to coassemble into the axoneme of transgenic flies. *Eur. J. Cell. Biol.*, **54**, 110–120.
6. Joshi, H.C. and Cleveland, D.W. (1989) Differential utilization of beta-tubulin isotypes in differentiating neurites. *J. Cell Biol.*, **109**, 663–673.
7. Burgoyne, R.D., Cambray-Deakin, M.A., Lewis, S.A., Sarkar, S. and Cowan, N.J. (1988) Differential distribution of beta-tubulin isotypes in cerebellum. *EMBO. J.*, **7**, 2311–2319.
8. Cleveland, D.W. (1987) The multitubulin hypothesis revisited: what have we learned? *J. Cell Biol.*, **104**, 381–383.
9. Tischfield, M.A. and Engle, E.C. (2010) Distinct alpha- and beta-tubulin isotypes are required for the positioning, differentiation and survival of neurons: new support for the 'multi-tubulin' hypothesis. *Biosci. Rep.*, **30**, 319–330.
10. Jaglin, X.H., Poirier, K., Saillour, Y., Buhler, E., Tian, G., Bahi-Buisson, N., Fallet-Bianco, C., Phan-Dinh-Tuy, F., Kong, X.P., Bomont, P. *et al.* (2009) Mutations in the beta-tubulin gene TUBB2B result in asymmetrical polymicrogyria. *Nature Genet.*, **41**, 746–752.
11. Tischfield, M.A., Baris, H.N., Wu, C., Rudolph, G., Van Maldergem, L., He, W., Chan, W.M., Andrews, C., Demer, J.L., Robertson, R.L. *et al.* (2010) Human TUBB3 mutations perturb microtubule dynamics, kinesin interactions, and axon guidance. *Cell*, **140**, 74–87.
12. Guerrini, R., Mei, D., Cordelli, D.M., Pucatti, D., Franzoni, E. and Parrini, E. (2012) Symmetric polymicrogyria and pachygyria associated with TUBB2B gene mutations. *Eur. J. Hum. Genet.*, **20**, 995–998.
13. Poirier, K., Saillour, Y., Bahi-Buisson, N., Jaglin, X.H., Fallet-Bianco, C., Nabbout, R., Castelnau-Ptakhine, L., Roubertie, A., Attie-Bitach, T., Desguerre, I. *et al.* (2010) Mutations in the neuronal ss-tubulin subunit TUBB3 result in malformation of cortical development and neuronal migration defects. *Hum. Mol. Gen.*, **19**, 4462–4473.
14. Romaniello, R., Tonelli, A., Arrigoni, F., Baschirotto, C., Triulzi, F., Bresolin, N., Bassi, M.T. and Borgatti, R. (2012) A novel mutation in the beta-tubulin gene TUBB2B associated with complex malformation of cortical development and deficits in axonal guidance. *Dev. Med. Child Neurol.*, **54**, 765–769.
15. Tischfield, M.A., Cederquist, G.Y., Gupta, M.L. Jr and Engle, E.C. (2011) Phenotypic spectrum of the tubulin-related disorders and functional implications of disease-causing mutations. *Curr. Opin. Genet. Dev.*, **21**, 286–294.
16. Demer, J.L., Clark, R., Tischfield, M.A. and Engle, E.C. (2010) Magnetic Resonance Imaging Evidence Of an Asymmetrical Endophenotype in Congenital Fibrosis of Extraocular Muscles Type 3 Resulting from TUBB3 Mutations. *Invest. Ophthalmol. Vis. Sci.*, **51**, 4600–4611.
17. Doherty, E.J., Macy, M.E., Wang, S.M., Dykeman, C.P., Melanson, M.T. and Engle, E.C. (1999) CFEOM3: a new extraocular congenital fibrosis syndrome that maps to 16q24.2-q24.3. *Invest. Ophthalmol. Vis. Sci.*, **40**, 1687–1694.
18. Mackey, D.A., Chan, W.M., Chan, C., Gillies, W.E., Brooks, A.M., O'Day, J. and Engle, E.C. (2002) Congenital fibrosis of the vertically acting extraocular muscles maps to the FEOM3 locus. *Hum. Genet.*, **110**, 510–512.
19. Jaglin, X.H. and Chelly, J. (2009) Tubulin-related cortical dysgeneses: microtubule dysfunction underlying neuronal migration defects. *Trends Genet.*, **25**, 555–566.
20. Flaherty, M.P., Grattan-Smith, P., Steinberg, A., Jamieson, R. and Engle, E.C. (2001) Congenital fibrosis of the extraocular muscles associated with cortical dysplasia and maldevelopment of the basal ganglia. *Ophthalmology*, **108**, 1313–1322.
21. Li, H., DeRosier, D.J., Nicholson, W.V., Nogales, E. and Downing, K.H. (2002) Microtubule structure at 8 A resolution. *Structure*, **10**, 1317–1328.
22. Lowe, J., Li, H., Downing, K.H. and Nogales, E. (2001) Refined structure of alpha beta-tubulin at 3.5 A resolution. *J. Mol. Biol.*, **313**, 1045–1057.
23. Uchimura, S., Oguchi, Y., Hachikubo, Y., Ishiwata, S. and Muto, E. (2010) Key residues on microtubule responsible for activation of kinesin ATPase. *EMBO. J.*, **29**, 1167–1175.
24. Uchimura, S., Oguchi, Y., Katsuki, M., Usui, T., Osada, H., Nikawa, J., Ishiwata, S. and Muto, E. (2006) Identification of a strong binding site for kinesin on the microtubule using mutant analysis of tubulin. *EMBO. J.*, **25**, 5932–5941.
25. Wang, C.L., Zhang, L., Zhou, Y., Zhou, J., Yang, X.J., Duan, S.M., Xiong, Z.Q. and Ding, Y.Q. (2007) Activity-dependent development of callosal projections in the somatosensory cortex. *J. Neurosci.*, **27**, 11334–11342.
26. Adesnik, H. and Scanziani, M. (2010) Lateral competition for cortical space by layer-specific horizontal circuits. *Nature*, **464**, 1155–1160.
27. Kalil, K., Li, L. and Hutchins, B.I. (2011) Signaling mechanisms in cortical axon growth, guidance, and branching. *Front. Neuroanat.*, **5**, 62.
28. Halloran, M.C. and Kalil, K. (1994) Dynamic behaviors of growth cones extending in the corpus callosum of living cortical brain slices observed with video microscopy. *J. Neurosci.*, **14**, 2161–2177.
29. Gupta, M.L. Jr, Carvalho, P., Roof, D.M. and Pellman, D. (2006) Plus end-specific depolymerase activity of Kip3, a kinesin-8 protein, explains its role in positioning the yeast mitotic spindle. *Nat. Cell. Biol.*, **8**, 913–923.
30. Varga, V., Helenius, J., Tanaka, K., Hyman, A.A., Tanaka, T.U. and Howard, J. (2006) Yeast kinesin-8 depolymerizes microtubules in a length-dependent manner. *Nat. Cell. Biol.*, **8**, 957–962.
31. Gupta, M.L. Jr, Bode, C.J., Thrower, D.A., Pearson, C.G., Suprenant, K.A., Bloom, K.S. and Himes, R.H. (2002) beta-Tubulin C354 mutations that severely decrease microtubule dynamics do not prevent nuclear migration in yeast. *Mol. Biol. Cell.*, **13**, 2919–2932.
32. Yamada, K., Andrews, C., Chan, W.M., McKeown, C.A., Magli, A., De Berardinis, T., Loewenstein, A., Lazar, M., O'Keefe, M., Letson, R. *et al.* (2003) Heterozygous mutations of the kinesin KIF21A in congenital fibrosis of the extraocular muscles type 1 (CFEOM1). *Nature Genet.*, **35**, 318–321.
33. Keeble, T.R., Halford, M.M., Seaman, C., Kee, N., Macheda, M., Anderson, R.B., Stacker, S.A. and Cooper, H.M. (2006) The Wnt receptor Ryk is required for Wnt5a-mediated axon guidance on the contralateral side of the corpus callosum. *J. Neurosci.*, **26**, 5840–5848.
34. Hutchins, B.I., Li, L. and Kalil, K. (2011) Wnt/calcium signaling mediates axon growth and guidance in the developing corpus callosum. *Dev. Neurobiol.*, **71**, 269–283.
35. Kalil, K. and Dent, E.W. (2005) Touch and go: guidance cues signal to the growth cone cytoskeleton. *Curr. Opin. Neurobiol.*, **15**, 521–526.
36. Li, L., Hutchins, B.I. and Kalil, K. (2009) Wnt5a induces simultaneous cortical axon outgrowth and repulsive axon guidance through distinct signaling mechanisms. *J. Neurosci.*, **29**, 5873–5883.
37. Ageta-Ishihara, N., Takemoto-Kimura, S., Nonaka, M., Adachi-Morishima, A., Suzuki, K., Kamijo, S., Fujii, H., Mano, T., Blaeser, F., Chatila, T.A. *et al.* (2009) Control of cortical axon elongation by a GABA-driven Ca2+/calmodulin-dependent protein kinase cascade. *J. Neurosci.*, **29**, 13720–13729.
38. Nakamura, Y., Yamamoto, M., Oda, E., Yamamoto, A., Kanemura, Y., Hara, M., Suzuki, A., Yamasaki, M. and Okano, H. (2003) Expression of tubulin beta II in neural stem/progenitor cells and radial fibers during human fetal brain development. *Lab. Invest.*, **83**, 479–489.
39. Rakic, P. (1990) Principles of neural cell migration. *Experientia*, **46**, 882–891.
40. Noctor, S.C., Flint, A.C., Weissman, T.A., Dammerman, R.S. and Kriegstein, A.R. (2001) Neurons derived from radial glial cells establish radial units in neocortex. *Nature*, **409**, 714–720.
41. Kriegstein, A.R. and Noctor, S.C. (2004) Patterns of neuronal migration in the embryonic cortex. *Trends Neurosci.*, **27**, 392–399.

Downloaded from http://hmg.oxfordjournals.org/ at Serials Department on January 4, 2013

42. Noctor, S.C., Martinez-Cerdeno, V., Ivic, L. and Kriegstein, A.R. (2004) Cortical neurons arise in symmetric and asymmetric division zones and migrate through specific phases. *Nature Neurosci.*, **7**, 136–144.
43. Anton, E.S., Cameron, R.S. and Rakic, P. (1996) Role of neuron-glial junctional domain proteins in the maintenance and termination of neuronal migration across the embryonic cerebral wall. *J. Neurosci.*, **16**, 2283–2293.
44. Anton, E.S., Kreidberg, J.A. and Rakic, P. (1999) Distinct functions of alpha3 and alpha(v) integrin receptors in neuronal migration and laminar organization of the cerebral cortex. *Neuron*, **22**, 277–289.
45. Gongidi, V., Ring, C., Moody, M., Brekken, R., Sage, E.H., Rakic, P. and Anton, E.S. (2004) SPARC-like 1 regulates the terminal phase of radial glia-guided migration in the cerebral cortex. *Neuron*, **41**, 57–69.
46. Guerrini, R., Dobyns, W.B. and Barkovich, A.J. (2008) Abnormal development of the human cerebral cortex: genetics, functional consequences and treatment options. *Trends Neurosci.*, **31**, 154–162.
47. Manzini, M.C. and Walsh, C.A. (2011) What disorders of cortical development tell us about the cortex: one plus one does not always make two. *Curr. Opin. Genet. Dev.*, **21**, 333–339.
48. Ross, M.E. and Walsh, C.A. (2001) Human brain malformations and their lessons for neuronal migration. *Annu. Rev. Neurosci.*, **24**, 1041–1070.
49. Cappello, S., Bohringer, C.R., Bergami, M., Conzelmann, K.K., Ghanem, A., Tomassy, G.S., Arlotta, P., Mainardi, M., Allegra, M., Caleo, M. *et al.* (2012) A Radial Glia-Specific Role of RhoA in Double Cortex Formation. *Neuron*, **73**, 911–924.
50. Katsetos, C.D., Legido, A., Perentes, E. and Mork, S.J. (2003) Class III beta-tubulin isotype: a key cytoskeletal protein at the crossroads of developmental neurobiology and tumor neuropathology. *J. Child. Neurol.*, **18**, 851–866.
51. Jiang, Y.Q. and Oblinger, M.M. (1992) Differential regulation of beta III and other tubulin genes during peripheral and central neuron development. *J. Cell Sci.*, **103**, 643–651.
52. Wang, D., Villasante, A., Lewis, S.A. and Cowan, N.J. (1986) The mammalian beta-tubulin repertoire: hematopoietic expression of a novel, heterologous beta-tubulin isotype. *J. Cell Biol.*, **103**, 1903–1910.
53. Cross, D., Dominguez, J., Maccioni, R.B. and Avila, J. (1991) MAP-1 and MAP-2 binding sites at the C-terminus of beta-tubulin. Studies with synthetic tubulin peptides. *Biochemistry*, **30**, 4362–4366.
54. Littauer, U.Z., Giveon, D., Thierauf, M., Ginzburg, I. and Ponstingl, H. (1986) Common and distinct tubulin binding sites for microtubule-associated proteins. *PNAS*, **83**, 7162–7166.
55. Serrano, L., Wandosell, F., de la Torre, J. and Avila, J. (1986) Proteolytic modification of tubulin. *Methods Enzymol.*, **134**, 179–190.
56. Wandosell, F., Serrano, L., Hernandez, M.A. and Avila, J. (1986) Phosphorylation of tubulin by a calmodulin-dependent protein kinase. *J. Biol. Chem.*, **261**, 10332–10339.
57. Panda, D., Miller, H.P., Banerjee, A., Luduena, R.F. and Wilson, L. (1994) Microtubule dynamics *in vitro* are regulated by the tubulin isotype composition. *PNAS.*, **91**, 11358–11362.
58. Richards, K.L., Anders, K.R., Nogales, E., Schwartz, K., Downing, K.H. and Botstein, D. (2000) Structure-function relationships in yeast tubulins. *Mol. Biol. Cell.*, **11**, 1887–1903.
59. Hirokawa, N., Niwa, S. and Tanaka, Y. (2010) Molecular motors in neurons: transport mechanisms and roles in brain function, development, and disease. *Neuron*, **68**, 610–638.
60. Saito, T. (2006) *In vivo* electroporation in the embryonic mouse central nervous system. *Nat. Protoc.*, **1**, 1552–1558.
61. Saito, T. and Nakatsuji, N. (2001) Efficient gene transfer into the embryonic mouse brain using *in vivo* electroporation. *Dev. Biol.*, **240**, 237–246.
62. Fricker-Gates, R.A., Shin, J.J., Tai, C.C., Catapano, L.A. and Macklis, J.D. (2002) Late-stage immature neocortical neurons reconstruct interhemispheric connections and form synaptic contacts with increased efficiency in adult mouse cortex undergoing targeted neurodegeneration. *J. Neurosci.*, **22**, 4045–4056.
63. Gupta, M.L. Jr, Bode, C.J., Dougherty, C.A., Marquez, R.T. and Himes, R.H. (2001) Mutagenesis of beta-tubulin cysteine residues in Saccharomyces cerevisiae: mutation of cysteine 354 results in cold-stable microtubules. *Cell. Motil. Cytoskeleton*, **49**, 67–77.

Downloaded from http://hmg.oxfordjournals.org/ at Serials Department on January 4, 2013

Supplemental Materials:

An inherited *TUBB2B* mutation alters a kinesin binding site and causes polymicrogyria, CFEOM, and axon dysinnervation

Gustav Y. Cederquist,[*] Anna Luchniak,[*] Max A. Tischfield,[^] Maya Peeva,[^] Yuyu Song,[^] Manoj P. Menezes, Wai-Man Chan, Caroline Andrews, Sheena Chew, Robyn V. Jamieson, Lavier Gomes, Maree P. Flaherty, P. Ellen Grant, Mohan L. Gupta, Jr.,[#] Elizabeth Engle[#]

*equally contributing first authors

[^]equally contributing second authors

[#]co-corresponding authors

Contents:

Supplemental Methods

Clinical and Genetic Studies

A family with inherited CFEOM and PMG was enrolled in an ongoing genetic study of congenital cranial dysinnervation disorders (CCDDs). The study was conducted according to Declaration of Helsinki principles, approved by the Boston Children's Hospital Institutional Review Board, and written informed consent was obtained from each participant and/or his or her guardian. Medical records and testing results were provided. High molecular weight DNA was extracted from saliva samples using the purifier solution (DNA Genotek Inc., Kanata, Ontario, Canada). One affected family member was screened for mutations in all coding exons and exon-intron boundaries of *KIF21A, TUBB3, TUBB2B and TUBA1A* by Sanger sequencing. *KIF21A* and *TUBB3* were screened as previously described (1, 2), and screening conditions of *TUBB2B* and *TUBA1A* are available upon request. Co-segregation analysis was performed by sequencing additional participating family members. 336 control individuals (192 European-Caucasians, 96 Australians, and 48 mixed ethnicity) were screened for the presence of the pathogenic variant using denaturing high-performance liquid chromatography (dHPLC, Transgenomic, Inc. Omaha, Nebraska).

The haplotypes surrounding the *TUBB2B* locus were determined by running microsatellite markers D6S1600, D6S344, D6S1617, and D6S1713. Each amplicon was generated by 35 cycles of polymerase chain reaction using KAPA Fast Mastermix (KAPA Biosystems, Woburn, Massachusetts). Primer sequences were obtained from the UCSC Human Genome Browser (http://genome.ucsc.edu), and fluorescently labeled primers were purchased from Invitrogen (Carlsbad, California). The resulting fragments were run on a 3730 DNA analyzer, and genotyping data was analyzed using GeneMapper software (Applied Biosystems, Foster City, California). The haplotype map was generated using Progeny (Progeny Software LLC, Indianapolis, IN).

An additional 105 research participants (25 familial and 80 sporadic cases) with either CFEOM or another vertical CCDD who were mutation negative for *TUBB3* and *KIF21A* were identified, and their DNA Sanger sequenced for *TUBB2B.*

Mutation modeling

The *TUBB3* (2) and *TUBB2B* mutations were plotted on the solved protein structure of the $\alpha\beta$-tubulin heterodimer (Protein Data Bank [PDB] code 1JFF) using PyMOL software (1.1r1, http://www.pymol.org/).

Magnetic resonance imaging

The diagnostic structural and diffusion MRI scans for II:2 and II:3 were acquired at Westmead Hospital, Westmead, Australia on a 1.5T GE Signa HDxt scanner with the following sequence parameters:

1. High-resolution structural image: TR = 13.7ms; TE = 6.3 ms; 1mm isotropic scan.
2. DTI data: TR/TE = 6925/102.8 ms and 8000/104.8 ms; b=1000 s/mm^2, 1 image acquired with b=0, 13 diffusion directions, 1 x 1 in plane resolution, 5 mm slice thickness, 28 slices, 0mm gap-between-slices.

A structural and diffusion MRI of an age matched female control was acquired at Boston Children's Hospital, Boston, MA on a 3.0T Siemens TrioTim scanner with the following sequence parameters:

1. High-resolution structural image: TR = 2530 ms; TE = 1.66 ms; 1mm isotropic scan.
2. DTI data: TR/TE = 8000/104 ms; b=1000 s/mm^2, 10 images acquired with b=0 (only one of which was used for subsequent analysis to match the patient data), 13 diffusion directions, 1.1724 x 1.1724 in-plane resolution, 5mm slice thickness, 28 slices, 0mm gap-between-slices.

DTI data analysis for II:2, II:3, and healthy control. Interpretation was performed at Boston Children's Hospital, Boston, MA. DTI data were processed using a streamline algorithm for diffusion tractography using the Diffusion Toolkit developed at the Athinoula A. Martinos Center for Biomedical Imaging, Department of Radiology, Massachusetts General Hospital (Ruopeng Wang, Van J. Wedeen, TrackVis.org; http://trackvis.org). As a first step we performed eddy-currents correction using FMRIB library tools (http://www.fmrib.ox.ac.uk/fsl/fdt/fdt_eddy.html) to correct for distortions induced by the gradient-coils and for simple head motion. The whole-head brain images were stripped from the skull and other non-brain tissue using the Brain Extraction Tool (http://www.fmrib.ox.ac.uk/fsl/bet2/). Resulting brains were checked manually for accuracy. As a second mask to exclude noise outside the brain, we used a volume for which values at each voxel were the average of all 13 diffusion volumes (one for each diffusion direction).

Diffusion tensor estimation and fractional anisotropy (FA) volumes reconstruction were performed using the standard linear least-squares fitting method (3). Whole-brain fibers were reconstructed using the 2nd-order Runge-Kutta method (4). Tracts were terminated either when the angle between two consecutive orientation vectors was greater than the given threshold of 35° or when fibers extended outside of the brain surface. Trajectories were displayed on a 3D workstation (TrackVis, http://trackvis.org). The color-coding of fibers is based on a standard RGB code (red: left-right; green: front-back; blue: superior-inferior).

Subsequently, we used the axial and sagittal views on all slices in which the CC was visible and a combination of color FA maps, non-color FA maps, and b0 images from each participant to manually segment fibers running through the corpus callosum (CC). The use of non-color FA maps and b0 images were employed for increased accuracy in fiber-segmentation, as aberrant fibers in the two patients did not display with the correct directional color code on the color-FA maps.

DTI data analysis for PMG patients. Preprocessing and data interpretation was performed at Boston Children's Hospital, Boston, MA. Distortions in the diffusion tensor images caused by eddy currents and simple head motions were corrected by the diffusion toolbox of the FSL package (www.fmrib.ox.ac.uk/fsl/fdt). Diffusion tensor models were estimated and the fractional anisotropy (FA) and the apparent diffuse coefficient (ADC) were calculated at each voxel. Whole-brain white matter fiber tracts were reconstructed in native diffusion space for each subject using the fiber assignment by continuous tracking (FACT) algorithm (5), embedded in the Diffusion Toolkit (trackvis.org) (Ruopeng Wang, Van J. Wedeen, TrackVis.org; http://trackvis.org). In this process, a single seed was placed in the center of each voxel, and the path was continued in the adjacent voxel, which minimized the path curvature. Tracking was terminated when the angle between two consecutive orientation vectors was greater than the given threshold of 45° or when both ends of the fibers extended outside of the white matter mask. Subsequently, we used the axial and sagittal views on several slices in which the CC was clearly visible and a combination of color FA maps and non-color FA maps from each PMG

patient to manually segment fibers running through the corpus callosum (CC). The color-coding of fibers is the same as for the TUBB2B patients and the healthy control and is based on a standard RGB code (red: left-right; green: front-back; blue: superior-inferior).

In Vivo Mouse Experiments

Animals. All experiments were carried out in accordance with protocols approved by the Children's Hospital Boston Institutional Animal Care and Use Committee and with institutional and federal guidelines. Timed pregnant CD1 female mice were obtained from Charles River Laboratories (Wilmington, Massachusetts). The day of vaginal plug detection was defined as embryonic day E0.5. The day of animal birth was designated as post-natal day P0. Animals were housed in a temperature-controlled room and maintained on a 12-hour light/dark cycle. Food and water were available *ad libitum*.

DNA Plasmids. Full-length mouse *Tubb3* and *Tubb2b* cDNAs were amplified by PCR from an embryonic mouse brain cDNA library. The reverse primers contained the sequence for the HA epitope tag. *Tubb3-HA* and *Tubb2b-HA* PCR products were inserted into the pEF1α-*ires-EGFP* plasmid, modified from Addgene (Cambridge, Massachusetts) plasmid 11154, and the resulting plasmids are referred to as *Tubb3-WT-HA* and *Tubb2b-WT-HA*. 1228G>A and 1261G>A single-site mutagenesis was performed to construct the *Tubb3-E410K-HA* and *Tubb2b-E421K-HA* expression plasmids (QuikChange II, Agilent Technologies, Santa Clara, California). Empty pEF1α-*ires-EGFP* vector was used for GFP-alone conditions (*GFP*). Membrane targeted GFP (mGFP) was inserted into the pEF1α-*myc-hisB* plasmid (Invitrogen, Carlsbad, California). The CMV/βActin-*ires-GFP* (CBIG) plasmid was kindly provided by C. Lois (University of Massachusetts). Plasmid requests can be made with record numbers given in Supplemental Table 2.

Constructs were validated using Sanger sequencing (GeneWiz, South Plainfield, New Jersey), western blot and immunocytochemistry. For western blot, HEK 293T cells were grown to 80% confluence in a 12-well tissue culture dish (BD Falcon, San Jose, California) and transfected using Lipofectamine 2000 (Invitrogen, Carlsbad, California) according to the manufacturer's protocol. Cell lysates were collected 24 hours later in 50μl of RIPA buffer (Boston Bioproducts, Ashland, Massachusetts) with 1mM EDTA (Boston Bioproducts, Ashland, Massachusetts) and protease/phosphatase inhibitor cocktail (ThermoScientific, Rockford, Illinois). Protein was denatured in LDS sample buffer (Invitrogen, Carlsbad, California), run on 4-12% denaturing Bis-Tris denaturing gel (Invitrogen, Carlsbad, California), and transferred to a nitrocellulose membrane (Invitrogen, Carlsbad, California), and incubated overnight in primary antibody. The next day membranes were incubated with secondary antibodies at a concentration of 1:10,000 at room temperature for 1 hour (goat anti-rabbit, Jackson Immunoresearch, West Grove, Pennsylvania). Antibody concentrations are as follows: rabbit anti-actin, 1:10,000 (Sigma, St. Louis, Missouri); rabbit anti-HA, 1:100,000 (Abcam, Cambridge, Massachusetts). Chemiluminescent substrate (Amersham ECL Plus, GE Healthcare Life Sciences, Pittsburgh, Pennsylvania) was added, and images were captured using a FujiFilm LAS-4000 with CCD camera (GE Healthcare Life Sciences, Pittsburgh, PA).

For immunocytochemistry of primary cell culture to verify constructs, E15.5 cortical progenitors were electroporated and given 2 days to grow *in vivo*. On E17.5, the GFP-positive area from the lateral telencephalic wall was dissected in ice-cold HBSS (Invitrogen, Carlsbad, California). Tissue was digested in 0.25% trypsin (Invitrogen, Carlsbad, California) at 37°C for 15 min, and inactivated with 10% fetal bovine serum/Neurobasal (Invitrogen, Carlsbad, California). Tissue

was gently triturated with Neurobasal/1x B27/1x penicillin-streptomycin/2mM Glutamate. Cells were plated at a density of 400 cells / mm^2, and allowed to grow for 2 days *in vitro*. Cells were extracted for 2 minutes with 37°C PHEM buffer (60 mM PIPES, 27 mM HEPES, 10 mM EGTA, 8.2 mM $MgSO_4$, pH 7.0) containing 0.1% triton and 2 μm paclitaxel (Sigma, St. Louis, Missouri), then fixed for 10 minutes with 0.5% glutaraldehyde at room temperature. Cells were then processed for immunofluorescence.

In Utero Cortical Electroporation. Approximately 1μl of endotoxin free DNA mixture was pressure injected into the embryonic lateral ventricle of deeply anesthetized pregnant dams. 5 mm platinum plate tweezer electrodes (Protech, Boerne, Texas) were used to electroporate DNA with five 45 mV pulses of 50 ms duration at 1 s intervals (BTX Harvard Apparatus, Holliston, Massachusetts). Electrodes were oriented to direct DNA into the neocortical ventricular zone. All DNA plasmids were mixed to a final concentration of 1μg/μl each, in 0.05% Fast Green (Sigma, St. Louis, Missouri) and 1x sterile PBS. Co-electroporation DNA mixtures were as follows:
GFP: *GFP* + CBIG + mGFP
Tubb3-WT-HA: *Tubb3-WT-HA* + CBIG + mGFP
Tubb3-E410K-HA: *Tubb3-E410K-HA* + CBIG + mGFP
Tubb2b-WT-HA: *Tubb2b-WT-HA* + CBIG + mGFP
Tubb2b-E421K-HA: *Tubb2b-E421K-HA* + CBIG + mGFP

Histology. Brains were harvested at P2, P6, or P14. Transcardial perfusion with PBS followed by 4% PFA/PBS was done before fixing postnatal brains overnight in 4% PFA/PBS at 4°C. Brains were then sunk in 30% sucrose at 4°C and 50 μm floating sections were cut using a cryostat (Leica, Buffalo Grove, Illinois). Sections were stored in 0.0025% Sodium Azide/PBS at 4°C.

Immunocytochemistry. Floating 50 μm sections or primary cells were blocked at room temperature for 1 hour in goat block (8% goat serum (Equitech-Bio, Kerrville, Texas), 0.3% BSA (Sigma, St. Louis, Missouri), 0.3% Triton X-100 (Bio-Rad, Hercules, California), 0.0025% Sodium Azide (Sigma, St. Louis, Missouri), in PBS. Samples were then incubated overnight at 4°C in primary antibody diluted in goat block. Primary antibody concentrations are as follows: rabbit anti-GFP, 1:750 (Invitrogen, Carlsbad, California); chicken anti-GFP, 1:500 (Abcam, Cambridge, Massachusetts); rabbit anti-HA, 1:1000 (Abcam, Cambridge, Massachusetts); rat anti-Ctip2, 1:500 (Abcam, Cambridge, Massachusetts); rabbit anti-Cux1, 1:200 (Abcam, Cambridge, Massachusetts); rabbit anti-Foxp2, 1:200 (Abcam, Cambridge, Massachusetts). The following day, sections were rinsed for 10 min in PBS, and then incubated with appropriate fluorescent secondary antibodies from the Alexa series (Invitrogen, Carlsbad, California) at room temperature for 3 hours. For DAPI staining, sections were incubated for 10 minutes following secondary antibody incubation at a DAPI concentration of 1ug/ml. Primary cells were incubated for 1 hour at room temperature. Finally, sections were rinsed 3 times with PBS for 10 minutes and mounted on slides using 0.5% propyl gallate (Sigma, St. Louis, Missouri), 20mM Tris pH 8.0 (Boston BioProducts, Ashland, Massachusetts), and 90% glycerol. Primary cells were mounted using Fluoromount (SouthernBiotech, Birmingham, Alabama).

Image acquisition. Sections were imaged using an upright Olympus BX51 epifluorescence microscope (Olympus, Center Valley, Pennsylvania) with Spot Xplorerer CCD camera and Spot Version 4.6 acquisition software (Diagnostic Instruments, Sterling Heights, Michigan). Primary neurons were imaged using an inverted Nikon Eclipse Ti epifluorescence microscope with

Coolsnap HQ2 camera (Photometrics, Tucson, Arizona) and Nikon Elements software (Nikon, Melville, New York).

Image Analysis. Midline crossing was quantified as the ratio of contralateral to ipsilateral axonal GFP intensity in the CC. 200 μm x 200 μm boxes were drawn at the apex of the CC in each hemisphere to encapsulate all GFP-positive fibers in the CC in a single section (schematic in Figure 4C). Equal size boxes were also drawn directly adjacent to these boxes to attain background values for each tissue sample. Intensity values for the CC and background were attained using ImageJ software (NIH), and background values were subtracted from CC values to measure axonal GFP signal intensity. Total intensities from 3 to 5 sections were summed for each N. Each N represents one embryo.

Ipsilateral interstitial branching was quantified as the proportion of total branching in layer V and layer VI that occurs in layer VI. First, all images were cropped to the same size (see Figure 6A). Next, to correct for background that represents primary axon fluorescence and tissue auto-fluorescence, average fluorescence intensity per pixel was calculated for layer VI, V, and IV. Since little, if any, branching occurs in layer IV, the layer IV value was subtracted from layer VI and layer V values before calculating branching proportions. The corrected layer VI and V values were then extrapolated to give a fluorescence value that correlates to the number of branches in each respective layer. The proportion of layer VI branching was calculated as fluorescence intensity of VI divided by fluorescence intensity of layer V and VI. Fluorescence intensities were calculated using ImageJ (NIH). Values from 2 to 4 sections were summed for each N. Each N represents one embryo. P values were obtained using a one-way ANOVA with post-hoc Tukey t test for multiple comparisons.

In vitro tubulin heterodimer formation and cycling

Construction of mammalian expression plasmids. The cDNA encoding the human *TUBB2B* gene was amplified by PCR from the Marathon-ready human fetal brain cDNA library (Clontech, Mountain View, California) without the stop codon. The *TUBB2B* sequence was recombined into the pDNR^{TM}221 (Invitrogen, Carlsbad, California) and subcloned into the pcDNA3.2/V5 DEST (Invitrogen, Carlsbad, California) in-frame with a C-terminal V5 epitope tag and with the start codon in the context of a suboptimal Kozak sequence. Disease associated mutations 514T>C (S172P), 795C>G (F265L), and 1261G>A (E421K) were introduced into *TUBB2B-WT-V5* plasmid using site-directed mutagenesis (Agilent Technologies, Santa Clara, California) according to the manufacturer's protocol. The mutant plasmids are designated as *TUBB2B-S172P-V5*, *TUBB2B-F265L-V5*, and *TUBB2B-E421K-V5* in the manuscript. Plasmid requests can be made with record numbers given in Supplemental Table 2. All constructs were verified by Sanger sequencing.

In vitro *tubulin expression, heterodimer formation, and heterodimer cycling.* The *in vitro* transcription and translation reactions were carried out in 25 μl of rabbit reticulocyte lysates (TnT T7 Quick Coupled Transcription/Translation System, Promega, Madison, Wisconsin) at 30°C for 90 minutes using 125ng of *TUBB2B-WT-V5*, *TUBB2B-S172P-V5*, and *TUBB2B-F265L-V5*, and 188.5ng *TUBB2B-E421K-V5* as starting material. *TUBB2B-E421K-V5* starting material was increased to normalize polypeptide production. Subsequently, the transcription/translation reactions were chased for 2hr at 30°C with 0.2 mg/ml of purified porcine brain tubulin, 3.5mM $MgCl_2$ and 2mM GTP. 2μl and 3.5μl aliquots from each reaction were analyzed by SDS-PAGE (Any kD Mini-PROTEAN TGX gel, Bio-Rad, Hercules, California) and Native-PAGE (Native-PAGE 4-16% Bis-Tris gels, Invitrogen, Carlsbad, California), respectively, followed by transfer

onto PVDF membranes (Thermo Scientific, Rockford, Illinois). WT and mutant TUBB2B αβ-heterodimers were detected using a mouse anti-V5 monoclonal antibody at a concentration of 1:5000 (Invitrogen, Carlsbad, California). The chemiluminescent signal was detected by X-ray film (Thermo Scientific, IL) using Alphatek Model AX200 (Alphatek Corporation, IL) and analyzed by ImageJ. The products of the transcription/translation reaction were then mixed with 10μM purified porcine tubulin and taken through a round of microtubule polymerization and depolymerization as previously described (6). At the end of each spin, aliquots containing an equal amount of material were removed from supernatant and pellet fractions and analyzed by SDS-PAGE and western blot as described above.

HeLa cell incorporation Assay

HeLa cells were plated at a density of 20,000 cells/well in a 24-well plate on glass coverslips in DMEM with 2 mM glutamine (Invitrogen, Carlsbad, California), 10% fetal calf serum (Invitrogen, Carlsbad, California), 2 mM pen/strep (Invitrogen, Carlsbad, California). 24 hours after plating, cells were transfected with Lipofectamine 2000 (Invitrogen, Carlsbad, California) with *TUBB2B-WT-V5* and *TUBB2B-E421K-V5* expression constructs. The following day, cells were fixed in ice-cold methanol (to extract soluble tubulin) at −20°C for 10 min, or, protein lysate was collected in 10mM HEPES with 1%SDS to determine total V5 protein expression by western blot. Cells were subsequently incubated with mouse anti-V5 antibody (Invitrogen, Carlsbad, California) at a concentration of 1:5000 or rabbit anti-V5 (Sigma, St. Louis, Missouri) at a concentration of 1:2000 overnight at 4ºC. The next day cells were rinsed with PBS and incubated with Alexa-546 anti-mouse secondary antibody (Invitrogen, Carlsbad, California) at a concentration of 1:1200 for 1 hour at room temperature. Cells were thoroughly rinsed with PBS to remove all excess antibody, then stained for 1 hour at room temperature with FITC-conjugated monoclonal DM1α (Sigma, St. Louis, Missouri) to visualize α-tubulin. Cells were rinsed with PBS and mounted with Fluoromount (SouthernBiotech, Birmingham, Alabama). HeLa cell microtubules were imaged using a Zeiss LSM 700 series laser scanning confocal microscope and images were acquired using Zen Software (Carl Zeiss MIcroImaging GmbH, Göttingen, Germany). For Western Blot, protein was denatured in LDS sample buffer (Invitrogen, Carlsbad, California), run on 4-12% denaturing Bis-Tris denaturing gel (Invitrogen, Carlsbad, California), and transferred to a PVDF membrane (Invitrogen, Carlsbad, California), and incubated overnight in primary antibody. The next day membranes were incubated with secondary antibodies at a concentration of 1:10,000 at room temperature for 1.5 hours (goat anti-mouse, Jackson Immunoresearch, West Grove, Pennsylvania). Antibody concentrations are as follows: rabbit anti-DM1α, 1:20,000 (Sigma, St. Louis, Missouri); mouse anti-V5, 1:20,000 (Invitrogen, Carlsbad, California). Chemiluminescent substrate (Amersham ECL Plus, GE Healthcare Life Sciences, Pittsburgh, Pennsylvania) was added, and images were captured using a FujiFilm LAS-4000 with CCD camera (GE Healthcare Life Sciences, Pittsburgh, PA).

Image Analysis. For quantitative immunofluorescence, images were acquired using an upright Olympus BX51 epifluorescence microscope (Olympus, Center Valley, Pennsylvania) with Spot Xplorerer CCD camera and Spot Version 4.6 acquisition software (Diagnostic Instruments, Sterling Heights, Michigan). V5 expression intensity was calculated using ImageJ software (NIH) as the average pixel intensity for each cell. Quantification of western blot bands was performed using ImageJ software (NIH). Total V5 protein expression was calculated as the ratio of average pixel intensity of the V5 band to the average pixel intensity of the pan-alpha tubulin band. Data is represented as E421K expression intensity relative to a WT expression of 1.

Yeast Experiments

Yeast plasmids and strains. The *TUBB3* (2) and *TUBB2B* corresponding mutations were introduced into *TUB2* through site-directed mutagenesis (Agilent Technologies, Santa Clara, California) of the pCS3 plasmid (7). The WT and mutant *tub2* constructs were verified by Sanger sequencing and transformed into wildtype diploid yeast cells as previously described (8). Strains expressing Kip3p-3YFP, Kip2p-3YFP, Tub2p-C354S, or GFP-Tub1p were generated as previously described (9-11).

Carbendazim assay. Cells were grown overnight in YPD media (1% yeast extract, 2% peptone, 2% dextrose). The following day, optical density (OD) of cultures at 600nm was measured to determine cell density. Equal concentrations of cells from each strain were plated at logarithmic dilutions on plates containing increasing concentrations of carbendazim. Carbendazim plates were prepared by addition of a 10mg/ml carbendazim (Sigma, St. Louis, MO) stock solution in ethanol to YPD-agarose media to obtain final concentrations of 4, 6, 9, 12, 15, 18 and 21 μg/ml. Cell growth was monitored for 72 hours at 24°C. Carbendazim resistance was assessed using the following scale: mild resistance or moderate resistance if colony growth did not exceed one or two logarithmic dilutions compared to WT, and strong resistance if colony growth was detected at more than three logarithmic dilutions compared to WT survival.

Yeast microtubule dynamics. Cells expressing GFP-Tub1 were grown overnight in synthetic complete (SC) media (0.67% yeast nitrogen base without amino acids, 2% dextrose, 0.5% casamino acids) with 0.1mg/ml adenine (Sigma, St. Louis, Missouri) at 30°C. The following day cells were diluted into fresh SC media supplemented with 0.2 mM adenine and grown to mid-log phase at 30°C. Cells were pelleted and resuspended in SC media with adenine and imaged at room temperature on an automated AxioImager M2 (Carl Zeiss MIcroImaging GmbH, Göttingen, Germany) microscope with a 63x Plan Fluor 1.4 N.A. objective with a Coolsnap HQ2 camera (Photometrics, Tucson, Arizona). Typically eight z-series images at 0.75 μm axial steps were acquired at 8-second intervals. Astral microtubule dynamics were analyzed as described previously (12). To calculate catastrophe and rescue frequency, only the time spent in growth and paused phase or time spent shortening was considered, respectively. *P* values were determined using an unpaired Student's t-test.

Analysis of Kip3-3YFP and Kip2-3YFP expression. WT and mutant cells expressing Kip3p-3YFP or Kip2p-3YFP were grown overnight in SC media without leucine at 30°C. The following morning, cells were diluted into fresh SC media without leucine and grown until mid-log phase at 30°C. Subsequently, cells were lysed in lysis buffer (50mM Tris-HCl pH 8.0, 150mM NaCl, 2mM $MgCl_2$, 4mM PMSF, 0.2% Tween-20 and protease inhibitors) using a beadbeater (BioSpec Products, Bartlesville, Oklahoma) and total protein concentration was determined by the Bradford method (Bio-Rad Protein Assay Dye Reagent Concentrate, Bio-Rad, Hercules, California). Samples were analyzed using NuPAGE 4-12% Bis-Tris gels (Invitrogen, Carlsbad, California) and transferred to a PVDF membrane. Kip3p-3YFP or Kip2p-3YFP was detected using a polyclonal anti-GFP antibody (ABM) at a concentration of 1:5000 and equivalent protein loading was verified using a monoclonal antibody against β-actin (Abcam, Cambridge, Massachusetts) at a concentration of 1:1000. The chemiluminescent signal was detected by X-ray film using Alphatek Model AX200 (Alphatek Corporation, IL).

Kip3-3YFP and Kip2-3YFP localization on microtubule plus ends. WT or mutant cells expressing CFP-Tub1p (α-tubulin) and Kip3p-3YFP or Kip2p-3YFP were grown in SC media with 0.2 mM adenine and without leucine. Single time point z-series images were merged into a maximum

projection image following deconvolution with the nearest neighbor algorithm in Slidebook software (Intelligent Imaging Innovations, Denver, Colorado). The plus ends of all visible microtubules from all cells in the field of view were marked with a circle of equal diameter and the average YFP intensity within the circle was calculated using Slidebook. The average background signal was determined by marking an identical circle in the cytosol near each microtubule plus end and subtracted from the values for plus-end YFP signal. For Kip3p-3YFP at least 3 clones and for Kip2p-3YFP at least 2 clones for WT and mutant strains were imaged and analyzed on at least 2 separate days. For Kip3p-3YFP localization in cells containing Tub2-C354S, 2 clones for WT and a single clone for Tub2-C354S were imaged and analyzed on 3 separate days.

Supplemental Table 1. Primer Sequences

Table lists all primers used for cloning and mutagenesis as described in supplemental methods.

cDNA cloning primer sequences	**Gene**	**Animal**		
F: 5'-AAGGAATTCACCACCATGAGGGAGATCGTG-3' R: 5'-AGAGTTAACTCAAGCGTAATCTGGAACATC GTATGGGTACTTGGGCCCCTGGGCTTC-3'	*Tubb3-HA*	Mouse		
F: 5'-AAGGAATTCACCACCATGCGAGAGATCGTG-3' R: 5'-AGAGTTAACTCAAGCGTAATCTGGAACATC GTATGGGTAAGCCTCATCCTCGCCCTC-3'	*Tubb2b-HA*	Mouse		
F: 5'-GGGGACAAGTTTGTACAAAAAAGCAGGCTTCGCCATG CGTGAGATCGTGCACATCC-3' R: 5'-GGGGACCACTTTGTACAAGAAAGCTGGGTCCGCCTC GTCCTCGCCCTC-3'	*TUBB2B*	Human		
Mutagenic primer sequences	**Gene**	**Animal**	**Base pair change**	**Amino acid change**
S: 5'-GAGATGGAGTTCACCAAGGCCGAGAGCAACA-3' AS: 5'-TGTTGCTCTCGGCCTTGGTGAACTCCATCTC-3'	*Tubb3-HA*	Mouse	1228G>A	E410K
S: 5'-GCAACATGAATGACCTGGTGTCTAAGTACCAGCAGT-3' AS: 5'-ACTGCTGGTACTTAGACACCAGGTCATTCATGTTGC-3'	*Tubb2b-HA*	Mouse	1261G>A	E421K
5'-CCTGGTGTCCAAGTACCAGCAG-3' 5'-CTGCTGGTACTTGGACACCAGG-3'	*TUBB2B*	Human	1261G>A	E421K
5'-CGTCATGCCCCCACCCAAGG-3' 5'-CCTTGGGTGGGGGCATGACG-3'	*TUBB2B*	Human	514T>C	S172P
5'-CGCCTGCACTTGTTCATGCCCG-3' 5'-CGGGCATGAACAAGTGCAGGCG-3'	*TUBB2B*	Human	795C>G	F265L
5'-GATCTGGTTAGCAAATACCAACAATA-3' 5'-TATTGTTGGTATTTGCTAACCAGATC-3'	*TUB2*	Yeast	1261G>A	E421K

Supplemental Table 2. Permanent record numbers for DNA plasmids

Table lists permanent record numbers for plasmid requests.

Record number	Vector	Inserted gene	Source	Detection tag
pMG484	pcDNA3.2/V5 DEST	*TUBB2B*	Human	V5
pMG485	pcDNA3.2/V5 DEST	*TUBB2B-S172P*	Human	V5
pMG486	pcDNA3.2/V5 DEST	*TUBB2B-F265L*	Human	V5
pMG487	pcDNA3.2/V5 DEST	*TUBB2B-E421K*	Human	V5
pMG488	pEF1α-ires-EGFP	*TUBB2B*	Mouse	HA
pMG489	pEF1α-ires-EGFP	*TUBB2B-E421K*	Mouse	HA
pMG490	pEF1α-ires-EGFP	*TUBB3*	Mouse	HA
pMG491	pEF1α-ires-EGFP	*TUBB3-E410K*	Mouse	HA
pMG21	PCS3 (7)	*TUB2*	S. cerevisiae	---
pMG493	PCS3	*TUB2-E410K*	S. cerevisiae	---
pMG494	PCS3	*TUB2-E421K*	S. cerevisiae	---

Supplemental Table 3. Permanent record numbers for yeast strains

Table lists permanent record numbers for yeast strain requests.

Strain	Relevant genotype
MGY682	*MATa/α, ura3/ura3*, *leu2/leu2*, *his3/his3*, *ade2/ade2*, *trp1/trp1*
MGY1099	*TUB2/TUB2-URA3*, otherwise isogenic to MGY682
MGY1100	*TUB2/tub2-E410K-URA3*, otherwise isogenic to MGY682
MGY1101	*TUB2/tub2-E421K-URA3*, otherwise isogenic to MGY682
MGY1102	*TUB2/TUB2-ura3::TRP1*, otherwise isogenic to MGY682
MGY1103	*TUB2/tub2-E410K-ura3::TRP1*, otherwise isogenic to MGY682
MGY1104	*TUB2/tub2-E421K-ura3::TRP1*, otherwise isogenic to MGY682
MGY1105, MGY1106, MGY1107	*TUB2/TUB2-ura3::TRP1*, *GFP-TUB1-URA3/ura3,* otherwise isogenic to MGY682
MGY1108, MGY1109, MGY1110	*TUB2/tub2-E410K-ura3::TRP1*, *GFP-TUB1-URA3/ura3,* otherwise isogenic to MGY682
MGY1111, MGY1112, MGY1113	*TUB2/tub2-E421K-ura3::TRP1*, *GFP-TUB1-URA3/ura3*, otherwise isogenic to MGY682
MGY 1114	*TUB2/TUB2-ura3::TRP1*, *CFP-TUB1-URA3/ura3*, otherwise isogenic to MGY682
MGY1115	*TUB2/tub2-E410K-ura3::TRP1*, *CFP-TUB1-URA3/ura3*, otherwise isogenic to MGY682
MGY1116	*TUB2/tub2-E421K-ura3::TRP1*, *CFP-TUB1-URA3/ura3*, otherwise isogenic to MGY682
MGY1117, MGY1118, MGY1119	*TUB2/TUB2-ura3::TRP1*, *CFP-TUB1-URA3/ura3, KIP3/KIP3-3YFP-LEU2*, otherwise isogenic to MGY682
MGY1120, MGY1121, MGY1122	*TUB2/tub2-E410K-ura3::TRP1*, *CFP-TUB1-URA3/ura3, KIP3/KIP3-3YFP-LEU2,* otherwise isogenic to MGY682
MGY1123, MGY1124, MGY1125, MGY1126	*TUB2/tub2-E421K-ura3::TRP1*, *CFP-TUB1-URA3/ura3*, *KIP3/KIP3-3YFP-LEU2,* otherwise isogenic to MGY682
MGY1150, MGY1151	*TUB2/tub2-ura3::TRP1*, *CFP-TUB1-URA3/ura3, KIP2/KIP2-3YFP-LEU2*, otherwise isogenic to MGY682
MGY1152, MGY1153	*TUB2/tub2-E410K-ura3::TRP1*, *CFP-TUB1-URA3/ura3, KIP2/KIP2-3YFP-LEU2,* otherwise isogenic to MGY682
MGY1154, MGY1155. MGY1156	*TUB2/tub2-E421K-ura3::TRP1*, *CFP-TUB1-URA3/ura3*, *KIP2/KIP2-3YFP-LEU2,* otherwise isogenic to MGY682
MGY733	*TUB2/tub2::KanR,* otherwise isogenic to MGY682
MGY196	*MATa, tub2-C354S-ura3::HIS3, CFP-TUB1-URA3, Kip3-3YFP-LEU2, trp1*
MGY256, MGY257	*MATa, CFP-TUB1-URA3, Kip3-3YFP-LEU2, trp1, his3*

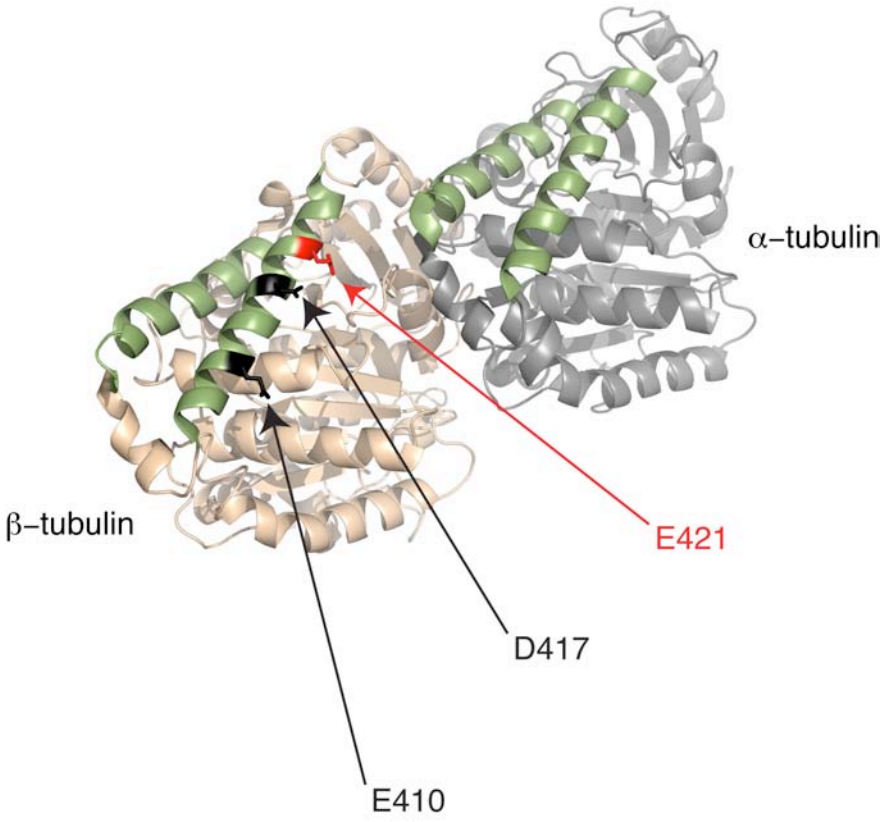

Supplemental Figure 1. *TUBB2B* 1261G>A nucleotide substitution alters the E421 kinesin binding residue

The H12 α-helix flanks the outer surface of tubulin, and is available for MAP and motor protein binding (green α-helices). Three charged residues, E410 (black), D417 (black), and E421 (red), which reside in the H12 α-helix, are required for high-affinity kinesin binding to the microtubule polymer (13). The *TUBB2B* 1261G>A mutation results in a non-conservative E>K amino acid substitution at residue E421. E410K, D417N, and D417H substitutions in *TUBB3* also result in CFEOM (2).

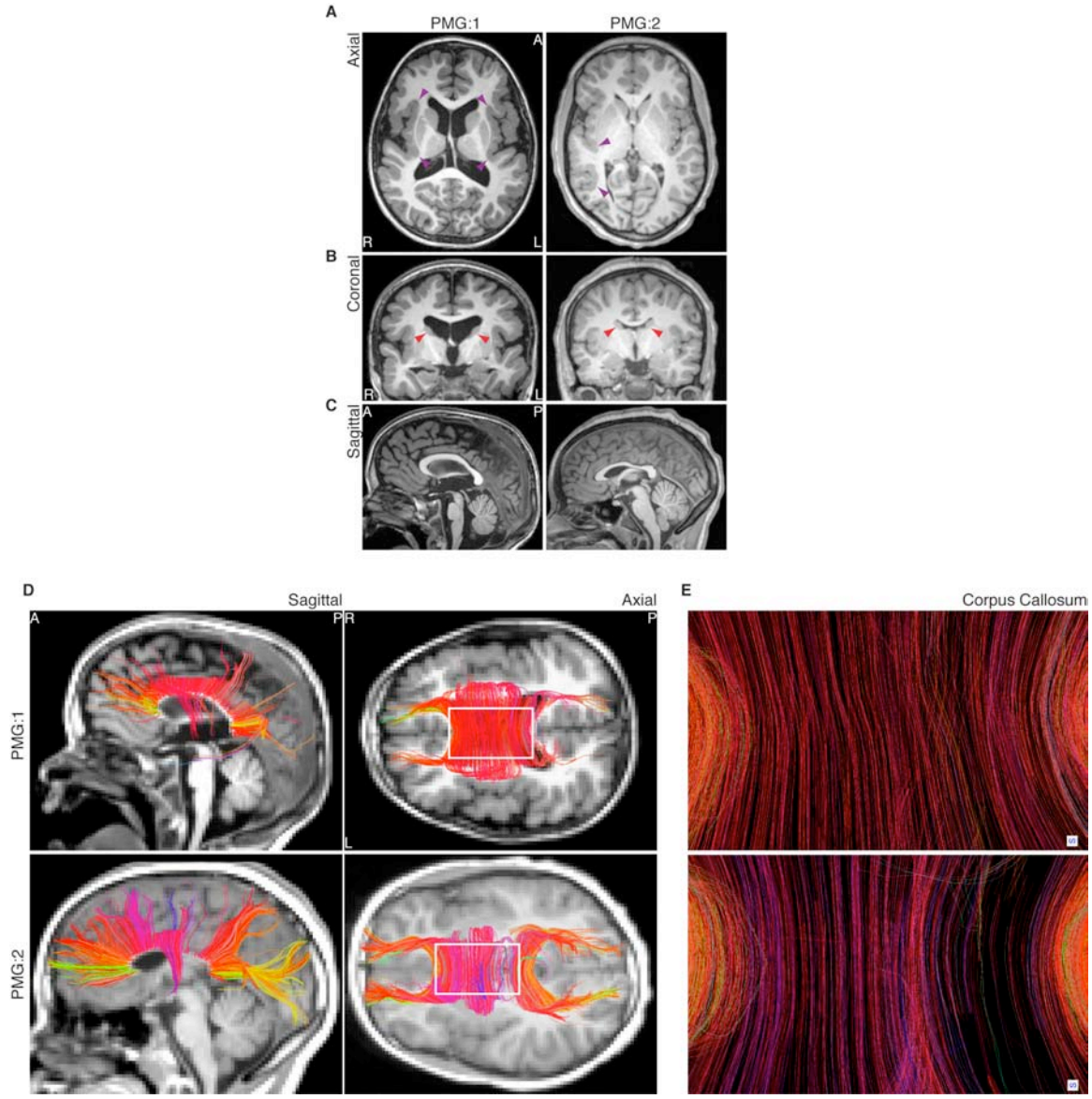

Supplemental Figure 2. Preserved homotopic connectivity in PMG patients without CFEOM

(A) Axial views show diffuse and bilateral PMG in PMG:1, and right predominant PMG in PMG:2 (purple arrowheads), with left sided involvement not seen on this image. **(B)** Coronal views show symmetric caudate bodies (red arrowheads). **(C)** Sagittal views show a completely formed CC with no gross abnormality in both PMG subjects. **(D)** DTI tractography reveals a paucity of CC fibers in both PMG subjects. The fibers are colored red, indicating a fairly preserved homotopic connectivity pattern. This is in contrast to the TUBB2B-E421K patients who had green commissural fibers, indicating disrupted homotopic connectivity. **(E)** Zoom in of the boxed region in (D) confirms that the homotopic connectivity pattern is preserved in PMG patients. PMG:1 (affected PMG patient 1), PMG:2 (affected PMG patient 2). PMG, polymicrogyria; CFEOM: congenital fibrosis of the extraocular muscles. L, left hemisphere; R, right hemisphere; A, anterior; P, posterior. CC, corpus callosum. Color-coding: red, left-right; green, anterior-posterior; blue, superior-inferior.

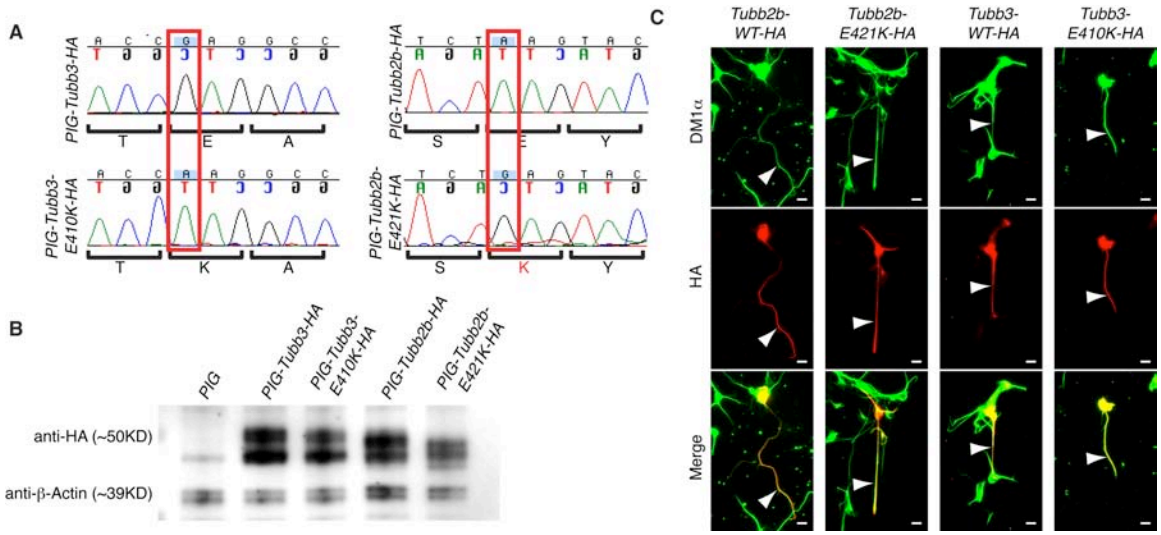

Supplemental Figure 3. Construct Validation

Plasmids generated to express wildtype and mutant tubulin alleles in mouse cortical neurons. **(A)** Sanger sequencing shows successful 1228G>A mutagenesis of the *Tubb3-WT-HA* plasmid to create *Tubb3-E410K-HA*, and 1261G>A mutagenesis of the *Tubb2b-WT-HA* plasmid to create *Tubb2b-E421K-HA*. **(B)** *GFP* alone, *Tubb3-WT-HA*, *Tubb3-E410K-HA*, *Tubb2b-WT-HA*, and *Tubb2b-E421K-HA* plasmids were transfected into HEK 293T cells. Western blot shows that the HA-tagged proteins are produced at the size expected for tubulin. Mutant tubulins are expressed at comparable, though slightly lower levels compared to respective WT controls. **(C)** *Tubb3-WT-HA*, *Tubb3-E410K-HA*, *Tubb2b-WT-HA*, and *Tubb2b-E421K-HA* plasmids were electroporated into cortical neurons at E15.5, and dissociated at E17.5. After 2 days *in vitro*, soluble tubulin was extracted with Triton X-100. The microtubules were fixed for immunocytochemistry of α-tubulin (DM1α, green, arrowheads) and HA-tagged β-tubulin (HA, red, arrowheads). Immunofluorescence shows co-localization of α-tubulin and HA-tagged β-tubulin (merge, yellow, arrowheads), showing that all constructs produce β-tubulin (red) that is capable of incorporating into neuronal microtubules. Viewed at least 20 cells for each condition, and the experiment was repeated on two different days. Scale bars: 20 μm.

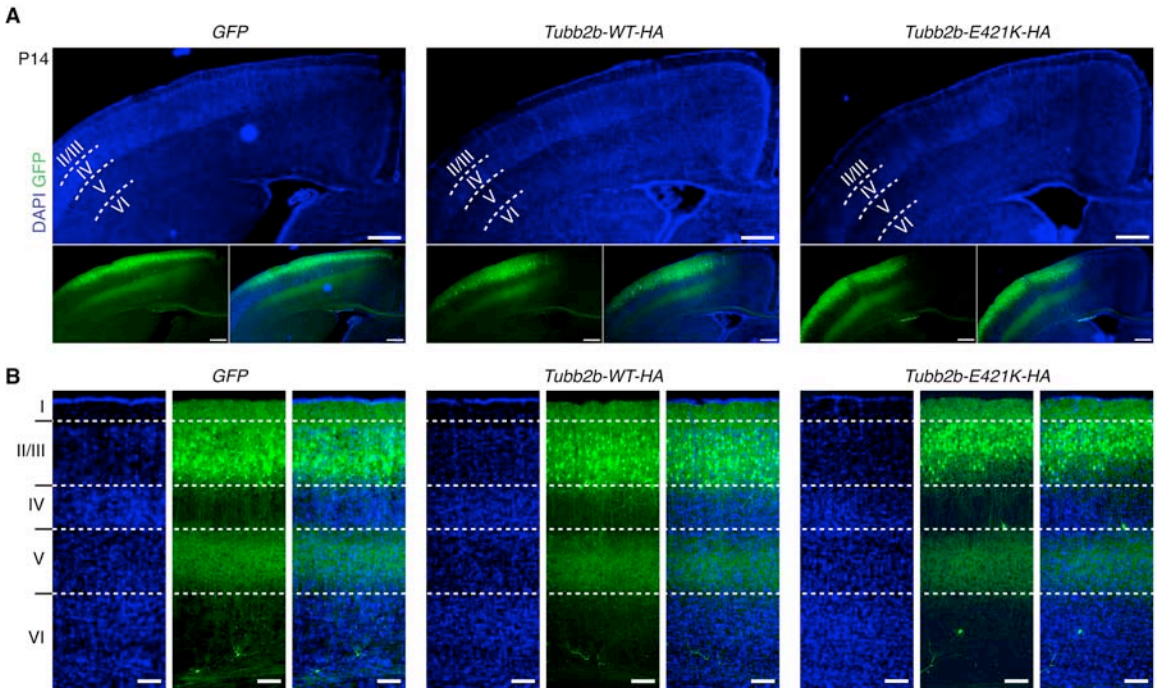

Supplemental Figure 4. Cortical cytoarchitecture and lamination is largely unaffected by overexpression of Tubb2b-E421K

Cortical neurons were electroporated at E15.5 and electroporated hemispheres were analyzed with DAPI at P14. **(A,B)** Low and high magnification images demonstrate that hemispheres electroporated with *GFP*, *Tubb2b-WT-HA*, or *Tubb2b-E421K-HA* have similar overall cortical thickness, have similar laminar thickness, and similar cellular densities within each layer. Importantly, high magnification images (B) indicate that *Tubb2b-E421K-HA* electroporated neurons migrate appropriately to layer II/III, and do not over-migrate into layer I or past the pia, as is sometimes observed in PMG patients. These high magnification images confirm that cellular densities in each layer are not altered by electroporation of *Tubb2b-E421K-HA*. N = 3 (*GFP*), N = 4 (*Tubb2-WT-HA*), N = 4 (*Tubb2b-E421K-HA*). N represents one embryo. PMG, polymicrogyria. Scale bars: 400 μm (A), 100 μm (B).

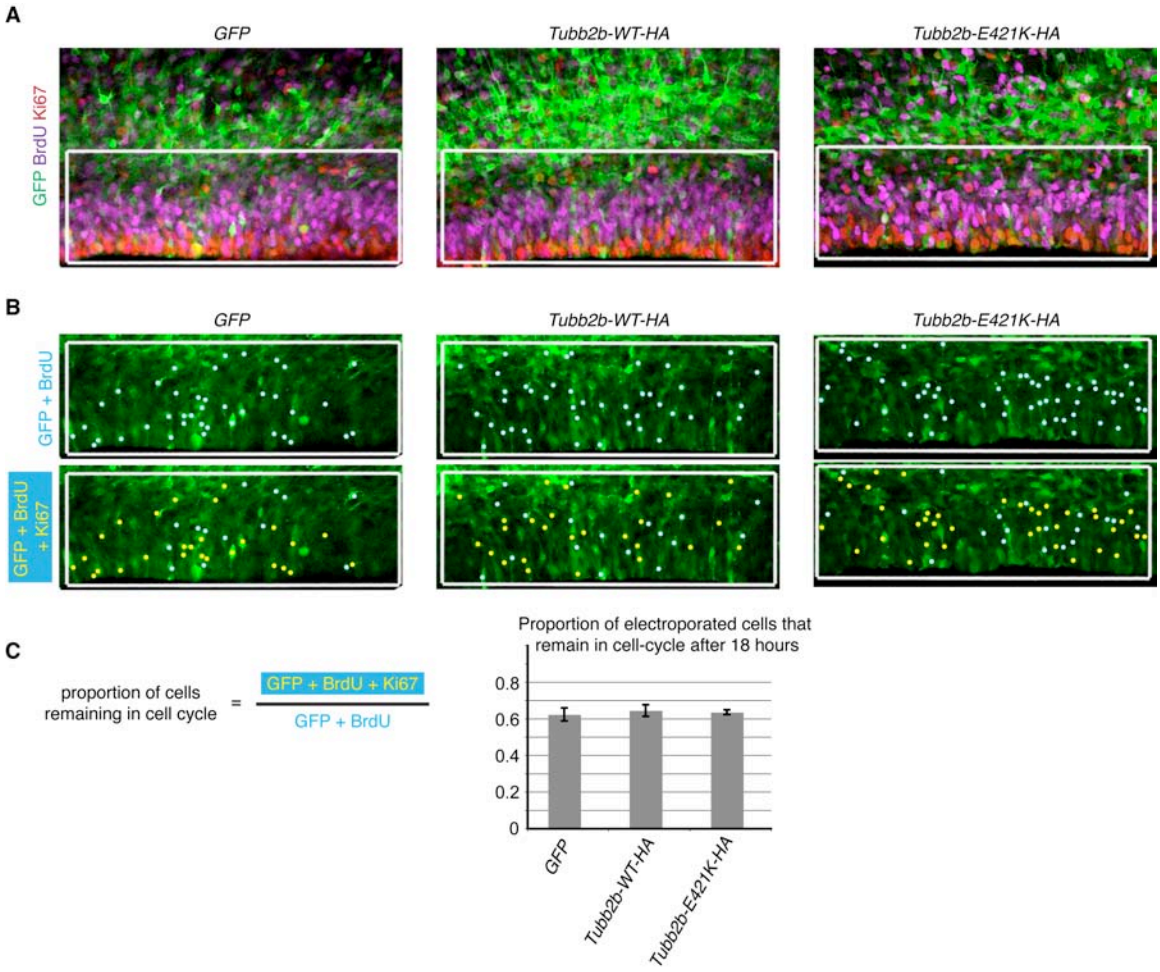

Supplemental Figure 5. Tubb2b-E421K overexpression does not alter duration of the cell cycle

Cortical neurons were electroporated at E15.5, pulsed with BrdU 24 hours later, and stained with Ki67 18 hours after BrdU injection. **(A)** Representative images of GFP (green), BrdU (purple), and Ki67 (red) immunostaining. Co-expressing cells were counted in boxed region. **(B)** Representative images of counting paradigm used for analysis. Cells expressing GFP and BrdU were marked with a blue dot, and the subset of cells also expressing Ki67 was marked with yellow dots. **(C)** There were no significant differences in the proportion of cells that remain in cell cycle between experimental conditions (*GFP* = 0.61±0.04, *Tubb2b-WT-HA* = 0.65±0.03, *Tubb2b-E421K-HA* = 0.62±0.01; P>0.05). The control values are in agreement with (14). N = 3 for all conditions. Cells from 3 to 6 sections were counted for each N. N represents one embryo. One-way ANOVA was used for multiple comparisons.

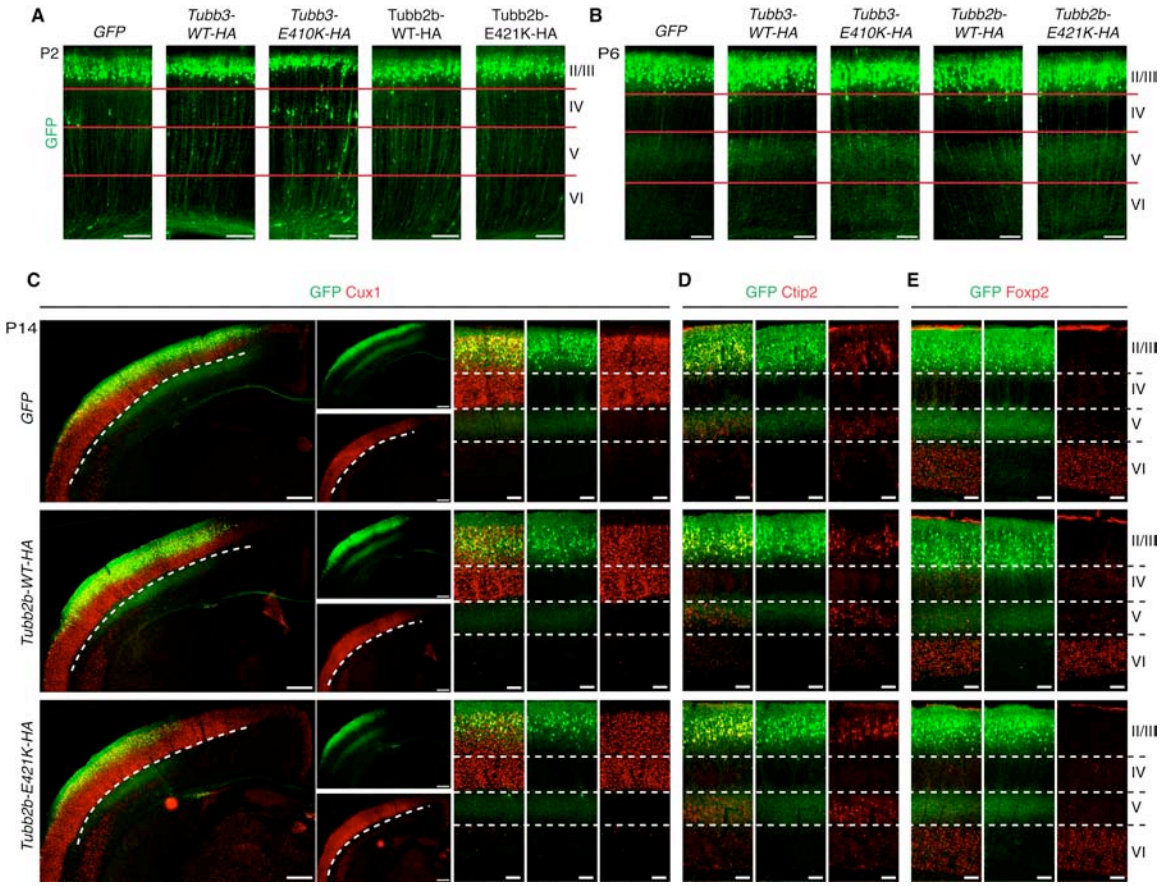

Supplemental Figure 6. Cortical neuron migration is largely unaffected by Tubb2b-E421K overexpression

Cortical neurons were electroporated at E15.5 and analyzed at P2, P6, and P14 for migratory abnormalities. **(A)** At P2, most upper layer cortical neurons electroporated with *GFP*, *Tubb3-WT-HA*, *Tubb3-E410K-HA*, *Tubb2b-WT-HA*, and *Tubb2b-E421K-HA* have reached the most superficial region of the cortical plate. A very small subset of neurons electroporated with *Tubb3-E410K-HA* has not reached the cortical plate at P2. **(B)** By P6, electroporated neurons in all conditions have reached layer II/III. **(C-E)** Overexpression of *Tubb2b-E421K-HA* does not perturb the laminar architecture of the cortex through P14. Cux1 expressing cells are largely confined to layer II/III (C). Ctip2 expressing cells are largely confined to layer V, except a small number of layer II/III cells which begin to express Ctip2 at mid to late postnatal stages (D). Foxp2 expressing cells are confined to layer VI (E). For P2, P6, and P14, respectively, N = 4,4,3 (*GFP*), N = 4,3 (*Tubb3-WT-HA*), N = 4,6 (*Tubb3-E410K-HA*), N = 4,5,4 (*Tubb2b-WT-HA*), N = 4,5,4 (Tubb2b-E421K-HA). N represents one embryo. Scale bars: 100 μm (A,B,C, D, E), 400 μm (C low magnification).

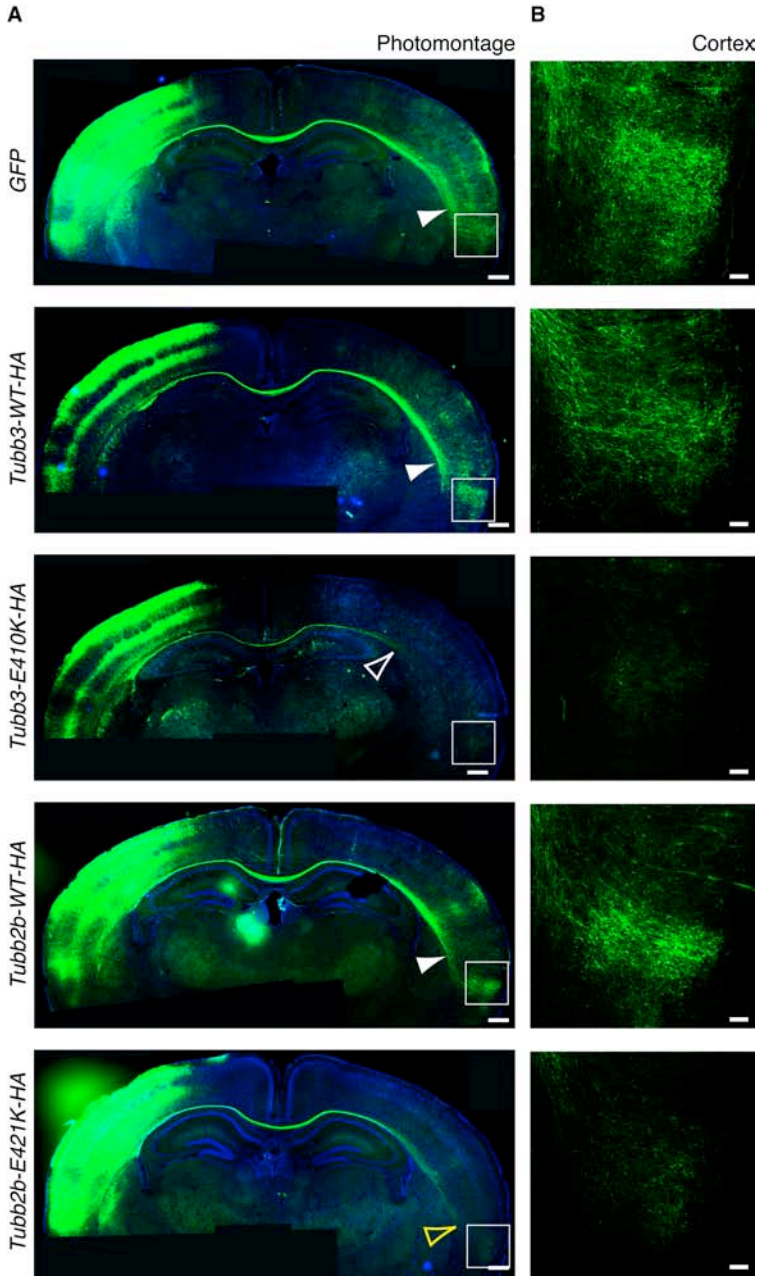

Supplemental Figure 7. Tubb2b-E421K-associated target innervation defects are maintained through P14

Cortical neurons were electroporated at E15.5 and analyzed at P14 to determine if the terminal axon extension defects observed at P6 represent a developmental delay or a failure of target innervation. **(A)** Photomontage of coronal sections show that *GFP, Tubb3-WT-HA, and Tubb2b-WT-HA* axons exhibit relatively uniform intensity and reach the most distal portion of the subcortical space (solid white arrowheads). The majority of *Tubb3-E410K-HA* CPN axons only reach the mid-lateral neocortical position (open white arrowhead). *Tubb2b-E421K-HA* CPN are relatively less affected, but still exhibit a marked reduction in the axons that reach the far-lateral subcortical space (open yellow arrowhead). **(B)** *GFP, Tubb3-WT-HA, and Tubb2b-WT-HA* electroporated neurons show dense innervation of the most lateral portion of the neocortical grey matter, while *Tubb3-E410K-HA* and *Tubb2b-E421K-HA* alleles result in severe reductions in grey matter innervation in the most lateral portion of the neocortical grey matter. N = 3 (*GFP*), N = 4 (*Tubb3-WT-HA*), N = 4 (*Tubb3-E410K-HA*), N = 3 (*Tubb2b-WT-HA*), N = 4 (*Tubb2b-E421K-HA*). N represents one embryo. Scale bars: 400 μm (A), 100 μm (B).

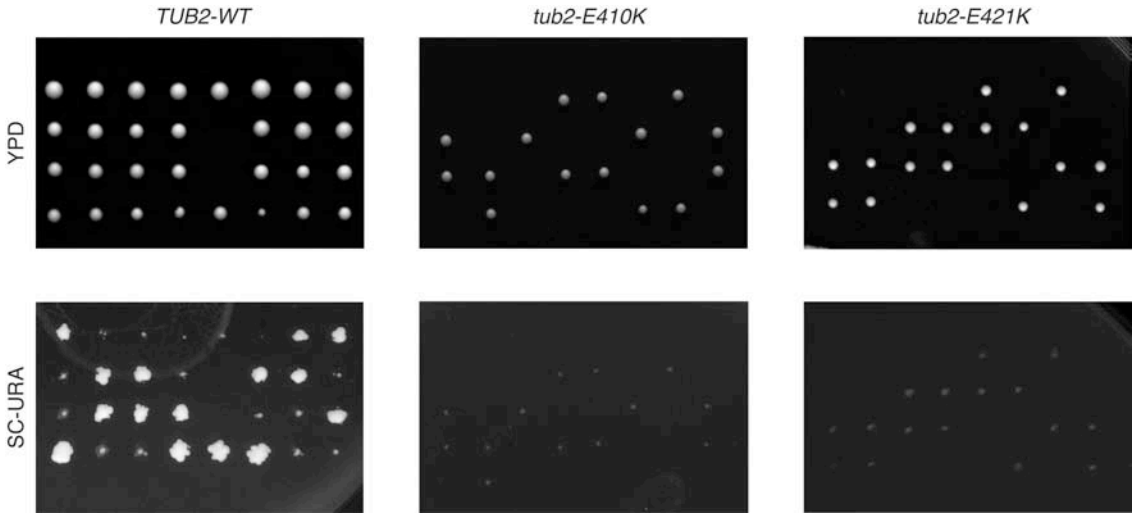

Supplemental Figure 8. *tub2-E421K* haploid spores are inviable

Tetrad analysis reveals that spores containing *tub2-E410K* or *tub2-E421K* as the sole source of β-tubulin are inviable. Diploid cells containing two copies of *TUB2* (WT) or heterozygous for *tub2-E410K* or *tub2-E421K* linked to URA (URA3) were sporulated, dissected (vertical quartets), and replica plated onto rich media (YPD) and media lacking uracil (SC-URA). Over 50 tetrads for each strain were dissected.

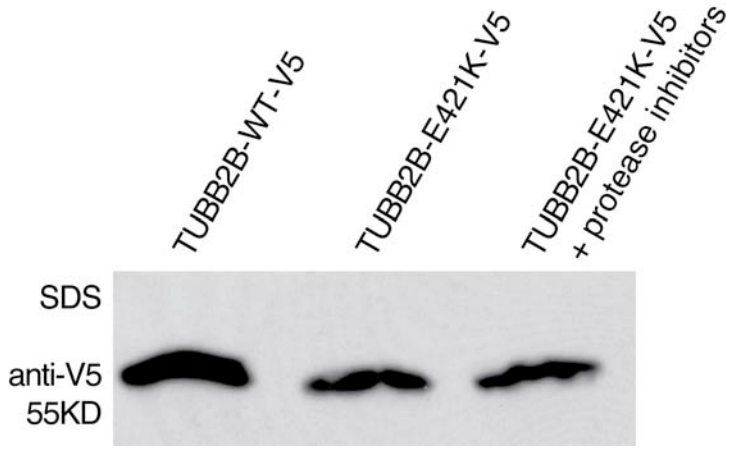

Supplemental Figure 9. *In vitro* transcription and/or translation efficiency of *TUBB2B-E421K-V5* is unaffected by protease inhibitors

Polypeptide production from *TUBB2B-WT-V5* cDNA is more robust than production from *TUBB2B-E421K-V5* cDNA (left and middle lanes). To determine if the reduced production is due to protein instability and degradation, *in vitro* transcription and translation were also performed in the presence of a protease inhibitor cocktail. The production of TUBB2B-E421K-V5 polypeptide is not changed in the presence of protease inhibitors (right lane).

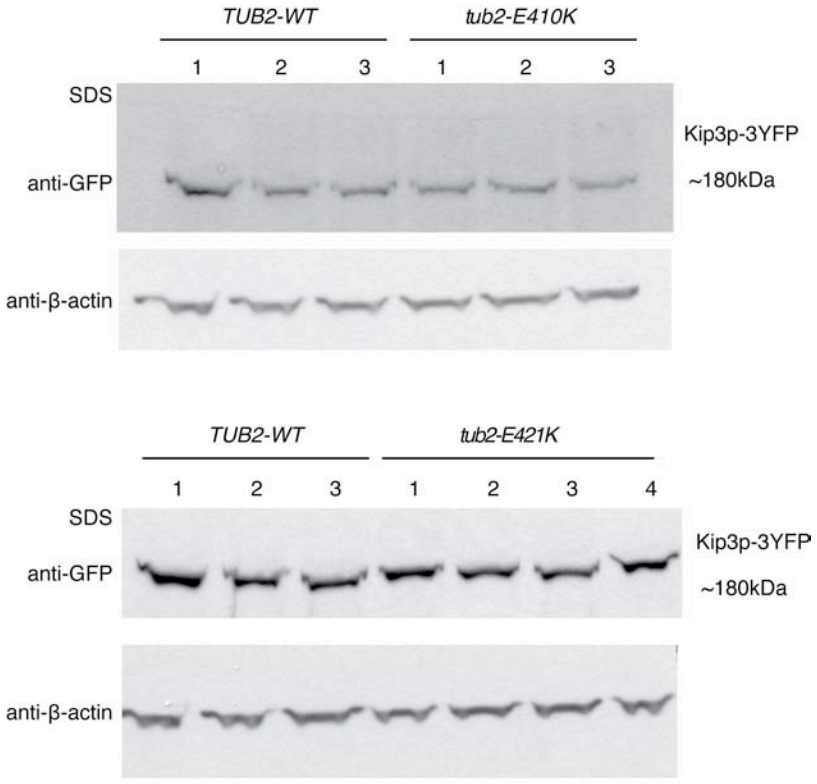

Supplemental Figure 10. Kip3p-3YFP levels are equivalent in yeast strains

Kip3p-3YFP protein levels are equivalent in analyzed *TUB2*, *tub2-E410K*, and *tub2-E421K* yeast strains. The strains used for quantification of Kip3p-3YFP on microtubule plus-ends were grown to log phase, lysed, and expression levels of Kip3p-3YFP fusion protein (~180kDa) levels were determined by western blotting with an anti-GFP antibody. β-actin levels were used to verify equal protein loading.

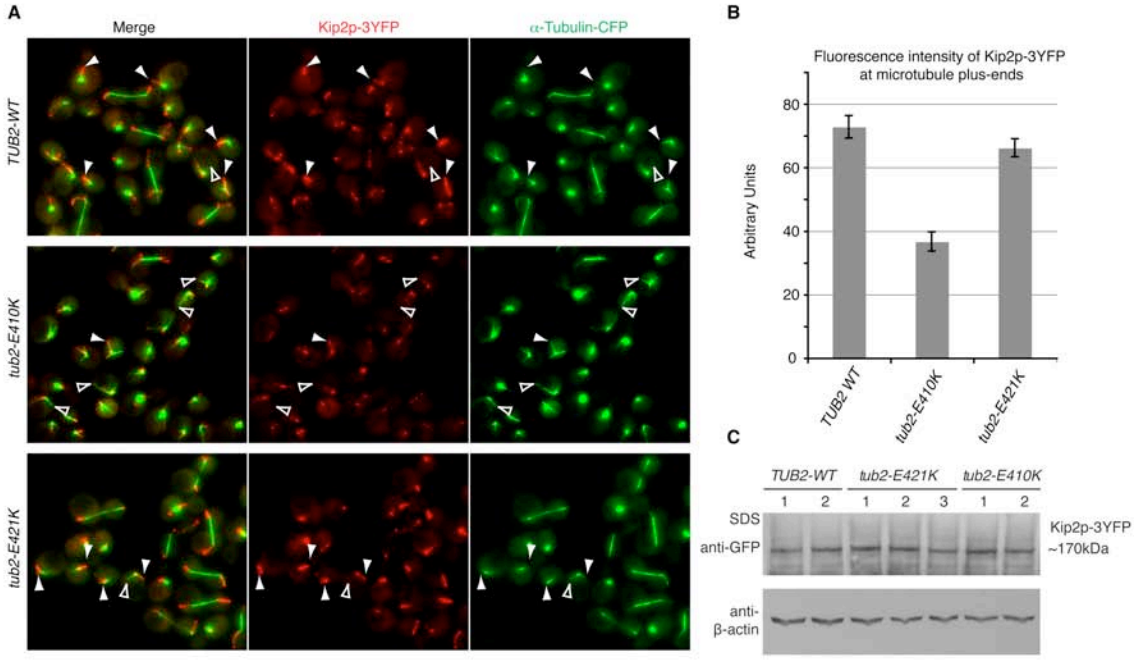

Supplemental Figure 11. Localization of kinesin Kip2p is not changed at microtubule plus-ends in *tub2-E421K* yeast

(A) Representative Z-series maximum projections showing fluorescently labeled Kip2p-3YFP (red) and α-tubulin (green) in live diploid *TUB2-WT*, heterozygous *tub2-E410K*, and heterozygous *tub2-E421K* yeast cells. Kip2p-3YFP forms bright foci at the plus-ends of most WT and E421K astral microtubules, but these bright foci are rarely found at the plus-ends of E410K astral microtubules (solid white arrowheads). Most astral microtubule plus-ends in *tub2-E410K* cells have Kip2p-3YFP foci, but with low intensity (open white arrowheads). Signal intensities were adjusted equally in both channels for all strains. **(B)** Quantification of Kip2p-3YFP levels at the plus-ends of microtubules in *TUB2-WT*, *tub2-E410K*, and *tub2-E421K*. Localization of Kip2p-3YFP intensity was reduced by 50% in *tub2-E410K* cells ($p<0.0005$), but not significantly reduced in *tub2-E421K* cells. *TUB2-WT* = 72.74±3.55, *tub2-E410K* = 36.63±3.04, *tub2-E421K* = 66.14±2.82. **(C)** Western blot of Kip2p-3YFP strains shows equal Kip2p-3YFP expression. 81 to 222 microtubules from 2 to 3 clones were analyzed on two separate days. N≥4 for all conditions. N represents the averaged values for a single clone on one day. Error represented as SEM in graphs. P value calculated by unpaired Student's t-test.

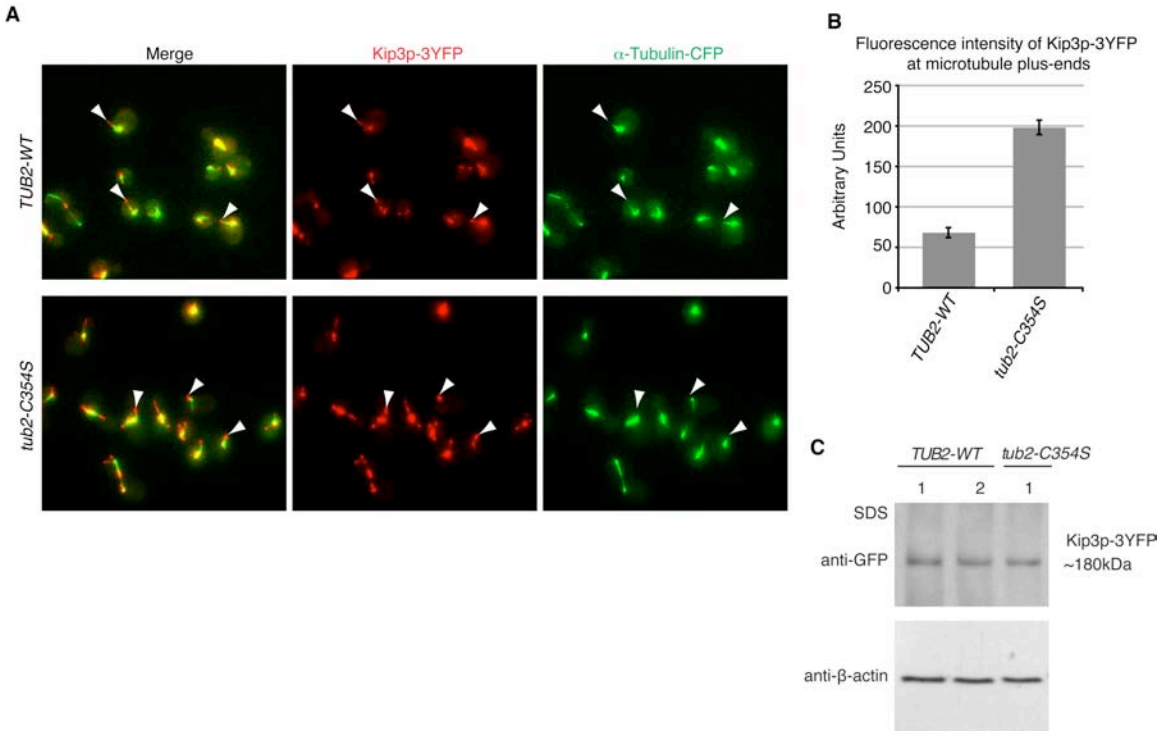

Supplemental Figure 12. Microtubule stabilization does not reduce the localization of kinesin Kip3p at microtubule plus-ends

(A) Representative Z-series maximum projections showing fluorescently labeled Kip3p-3YFP (red) and α-tubulin (green) in live diploid *TUB2-WT* and heterozygous *tub2-C354S* strains. Kip3-3YFP forms very bright foci at the plus-ends of most C354S astral microtubules (solid white arrowheads). **(B)** Quantification of Kip3p-3YFP levels at the plus-ends of microtubules in *TUB2-WT* or *tub2-C354S*. Localization of Kip3p-3YFP intensity was increased by 291% in *tub2-C354S* cells ($p<0.0005$), demonstrating that reduced Kip3p-3YFP levels in *tub2-E421K* strains is not secondary to microtubule stabilization. *TUB2-WT* = 68±6.22, *tub2-C354S* = 197.75±9.05. **(C)** Western blot of Kip3p-3YFP strains shows equal Kip3p-3YFP expression. 85 to 228 microtubules from 1 to 2 clones were analyzed on three separate days. N≥3 for all conditions. N represents the averaged values for a single clone on one day. Error represented as SEM in graphs. P value calculated by unpaired Student's t-test.

Supplemental Movie 1. *In vivo* dynamics of microtubules containing tub2p-E421K

Time-lapse microscopy of diploid G1 cells expressing WT *TUB2* (left column) or heterozygous for *tub2-E421K* (center column) or *tub2-E410K* (right column). Microtubules are labeled with GFP-Tub1p (α-tubulin). The magnification (63x), time-lapse interval (8s), and frame rate are identical for all cells. The entire time-lapse represents 400s.

Supplemental References

1 Yamada, K., Andrews, C., Chan, W.M., McKeown, C.A., Magli, A., De Berardinis, T., Loewenstein, A., Lazar, M., O'Keefe, M., Letson, R. *et al.* (2003) Heterozygous mutations of the kinesin KIF21A in congenital fibrosis of the extraocular muscles type 1 (CFEOM1). *Nature Genetics*, **35**, 318-321.
2 Tischfield, M.A., Baris, H.N., Wu, C., Rudolph, G., Van Maldergem, L., He, W., Chan, W.M., Andrews, C., Demer, J.L., Robertson, R.L. *et al.* (2010) Human TUBB3 mutations perturb microtubule dynamics, kinesin interactions, and axon guidance. *Cell*, **140**, 74-87.
3 Basser, P.J., Mattiello, J. and LeBihan, D. (1994) MR diffusion tensor spectroscopy and imaging. *Biophys J*, **66**, 259-267.
4 Lazar, M., Weinstein, D.M., Tsuruda, J.S., Hasan, K.M., Arfanakis, K., Meyerand, M.E., Badie, B., Rowley, H.A., Haughton, V., Field, A. *et al.* (2003) White matter tractography using diffusion tensor deflection. *Hum Brain Mapp*, **18**, 306-321.
5 Mori, S., Crain, B.J., Chacko, V.P. and van Zijl, P.C. (1999) Three-dimensional tracking of axonal projections in the brain by magnetic resonance imaging. *Ann Neurol*, **45**, 265-269.
6 Zabala, J.C. and Cowan, N.J. (1992) Tubulin dimer formation via the release of alpha- and beta-tubulin monomers from multimolecular complexes. *Cell Motil Cytoskeleton*, **23**, 222-230.
7 Sage, C.R., Davis, A.S., Dougherty, C.A., Sullivan, K. and Farrell, K.W. (1995) beta-Tubulin mutation suppresses microtubule dynamics in vitro and slows mitosis in vivo. *Cell Motil Cytoskeleton*, **30**, 285-300.
8 Gupta, M.L., Jr., Bode, C.J., Dougherty, C.A., Marquez, R.T. and Himes, R.H. (2001) Mutagenesis of beta-tubulin cysteine residues in Saccharomyces cerevisiae: mutation of cysteine 354 results in cold-stable microtubules. *Cell Motil Cytoskeleton*, **49**, 67-77.
9 Carvalho, P., Gupta, M.L., Jr., Hoyt, M.A. and Pellman, D. (2004) Cell cycle control of kinesin-mediated transport of Bik1 (CLIP-170) regulates microtubule stability and dynein activation. *Dev Cell*, **6**, 815-829.
10 Gupta, M.L., Jr., Carvalho, P., Roof, D.M. and Pellman, D. (2006) Plus end-specific depolymerase activity of Kip3, a kinesin-8 protein, explains its role in positioning the yeast mitotic spindle. *Nat Cell Biol*, **8**, 913-923.
11 Gupta, M.L., Jr., Bode, C.J., Thrower, D.A., Pearson, C.G., Suprenant, K.A., Bloom, K.S. and Himes, R.H. (2002) beta-Tubulin C354 mutations that severely decrease microtubule dynamics do not prevent nuclear migration in yeast. *Mol Biol Cell*, **13**, 2919-2932.
12 Tirnauer, J.S., O'Toole, E., Berrueta, L., Bierer, B.E. and Pellman, D. (1999) Yeast Bim1p promotes the G1-specific dynamics of microtubules. *J Cell Biol*, **145**, 993-1007.
13 Uchimura, S., Oguchi, Y., Katsuki, M., Usui, T., Osada, H., Nikawa, J., Ishiwata, S. and Muto, E. (2006) Identification of a strong binding site for kinesin on the microtubule using mutant analysis of tubulin. *EMBO J*, **25**, 5932-5941.
14 Siegenthaler, J.A., Ashique, A.M., Zarbalis, K., Patterson, K.P., Hecht, J.H., Kane, M.A., Folias, A.E., Choe, Y., May, S.R., Kume, T. *et al.* (2009) Retinoic acid from the meninges regulates cortical neuron generation. *Cell*, **139**, 597-609.